INSTITUTE OF PHYSICS PUBLISHING INVERSE PROBLEMS

Inverse Problems **20** (2004) 199–228 PII: S0266-5611(04)64221-3

An application of shape optimization in the solution of inverse acoustic scattering problems

Gonzalo R Feijóo[1,4], **Assad A Oberai**[2] **and Peter M Pinsky**[3]

[1] Sandia National Laboratories, Materials and Engineering Sciences Center, MS 9405, PO Box 0969, Livermore, CA 94551, USA
[2] Department of Aerospace and Mechanical Engineering, Boston University, 110 Cummington Street, Boston, MA 02215, USA
[3] Division of Mechanics and Computation, Durand Building room 269, Stanford University, Stanford, CA 94305-4040, USA

E-mail: grfeijo@sandia.gov

Received 30 May 2003, in final form 21 October 2003
Published 5 December 2003
Online at stacks.iop.org/IP/20/199 (DOI: 10.1088/0266-5611/20/1/012)

Abstract

We consider the problem of determining the shape of an object immersed in an acoustic medium from measurements obtained at a distance from the object. We recast this problem as a shape optimization problem where we search for the domain that minimizes a cost function that quantifies the difference between the measured and expected signals. The measured and expected signals are assumed to satisfy a boundary-value problem given by the Helmholtz equation with the Sommerfeld condition imposed at infinity. Gradient-based algorithms are used to solve this optimization problem. At every step of the algorithm the derivative of the cost function with respect to the parameters that describe the shape of the object is calculated. We develop an efficient method based on the adjoint equations to calculate the derivative and show how this method is implemented in a finite element setting. The predominant cost of each step of the algorithm is equal to one forward solution and one adjoint solution and therefore is independent of the number of parameters used to describe the shape of the object. Numerical examples showing the efficacy of the proposed methodology are presented.

(Some figures in this article are in colour only in the electronic version)

M This article features online multimedia enhancements

[4] Author to whom any correspondence should be addressed.

1. Introduction

Several problems in science and engineering can be posed as *optimization problems* with *constraints given by variational equations* or, equivalently, boundary-value problems. One such example is finding the shape of an object immersed in an unbounded acoustic medium given scattering information at certain locations and frequencies in the resonance region. In this *inverse acoustic scattering problem* the cost functional is the mismatch between the scattering pattern obtained from a trial solution and the measured one. The scattering pattern corresponding to the trial solution satisfies the wave equation with the Sommerfeld radiation condition imposed at infinity and appropriate boundary conditions imposed on the surface of the scatterer. This exterior acoustic boundary-value problem is a constraint imposed on the admissible scattering patterns. The 'variable' to be optimized is the shape of the scatterer, or equivalently, the domain where the boundary-value problem is posed.

On the other hand, the area of *mathematical programming*, or the solution of nonlinear constrained optimization problems in several variables, is very well developed, and there are several robust algorithms that can be used to treat different classes of problems. In this work, we pose the inverse acoustic scattering problem as a nonlinear constrained optimization problem in several variables and therefore, assuming that the functional and constraints are differentiable, we use these algorithms to efficiently find the optimum of the mathematical program which in turn gives the shape of the scatterer.

1.1. Algorithms used in the solution of the inverse acoustic scattering problem

The solution of inverse acoustic scattering problems for frequencies in the resonance region is a relatively new field in applied mathematics that has seen considerable growth in recent years. There are several algorithms that attempt to solve this problem. These algorithms, in general, fall into three classes.

The algorithms of the first class are linear and based on inverting a Fourier transform. The algorithms presented in [3] and [4] belong to this class. Methods of this type solve the inverse problem, which is intrinsically nonlinear, using a linear approximation (usually the Born approximation).

Another class of algorithms is given by the so-called 'linear sampling methods' based on the method of Colton and Kirsch [9]. This method has been analysed and extended in [6–8, 10, 11, 22, 23]. As observed by Brandfass [4], the methods of Colton and Kirsch are fundamentally single-frequency methods. There is no available procedure that allows the inclusion of information from illumination by plane waves of different frequencies.

The third category of algorithms used to solve the inverse acoustic scattering problem is given by gradient-based methods which are generally considered accurate but slow. In these algorithms, the inverse problem is formulated as an equation of the type $L(\partial\Omega_{\mathrm{B}}) = u_{\mathrm{T}}$ where L is the operator that assigns to every suitable boundary $\partial\Omega_{\mathrm{B}}$ the acoustic pattern u_{T} of the corresponding scattered wave. This equation is then solved by a Newton-type method and therefore requires the computation of the derivative of the operator L with respect to the domain Ω_{B}. In [21] Kirsch calculated this domain derivative. His method requires multiple solutions of the Helmholtz equation (one for each parameter used to describe the surface of the scatterer) in order to compute the domain derivative. In the numerical examples shown in that work, the boundary $\partial\Omega_{\mathrm{B}} \subset \mathbb{R}^2$ is assumed to be of star-like form. The shape of domains that can be represented using these curves is limited and therefore this algorithm is not able to represent accurately many types of scatterers.

Other authors [25, 30] also studied this third class of inverse scattering algorithms but in all those studies the domains being considered were of star-like form, the domain derivative

was calculated using an approach that requires the solution of a system of linear equations with a number of right-hand sides equal to the number of parameters used in the curve's representation, and the acoustic problem was solved using integral methods.

Still within the spirit of the methods of the third category, Santosa [33] developed an algorithm to solve inverse problems involving obstacles using a level-set approach. In his method, the obstacles are bounded by the zero value of an implicit function. Starting from an initial guess, the values of this function throughout the domain are updated by solving a Hamilton–Jacobi-type system. Upon convergence, obstacles are recovered as parts of the domain where the function attains negative values. Extensions of this methodology to other reconstruction problems were considered in [12, 26, 32]. In particular, in [26] and [32] the deformation of the level sets was related to a common operation in shape optimization, called the shape transformation. Methods using level sets are very general since the topology of the domain or the number of inclusions does not need to be known *a priori*. Nevertheless, these algorithms can be shown to use a steepest-descent direction to update the level set and solve the optimization problem. As a consequence, they require a greater number of iterations than methods that use Newton or quasi-Newton updates.

In [13] we proposed a method to solve inverse acoustic problems that falls in the third category of algorithms described above. In our method, we view the inverse problem as a shape optimization problem where the shape of the object that minimizes a functional that measures the error between the computed and measured acoustic patterns is sought. These acoustic patterns are assumed to be solutions of exterior acoustic problems which can then be viewed as constraints on the admissible values of the acoustic patterns. The solution of this constrained optimization problem is then accomplished using a quasi-Newton-type optimization algorithm that requires the computation of the shape derivative and satisfaction of the constraints. An auxiliary problem, called the adjoint problem, is solved in order to calculate the shape derivative efficiently. The acoustic and adjoint problems are solved using efficient finite element methods and iterative solvers. In this method, the number of scatterers has to be known in advance, nevertheless the shapes are represented by B-spline curves and therefore no other restricting assumptions on the geometry need be considered (star-shaped domains, for example).

The previous work was mainly limited to pure radiation conditions. Also, the proposed formulation was not computationally efficient for the case where the measured data was obtained many wavelengths away from the scatterer. In particular, it was not possible to consider the limiting case of measurements obtained in the far field. In this work we extend our previous method to treat these important cases. The proposed algorithm searches for the shape that minimizes a functional of the form

$$j(\Omega) = J(u_{\mathrm{s}}(\Omega)) = \tfrac{1}{2}\int_{\Gamma_{\mathrm{S}}} |u_{\mathrm{s}} - u_{\mathrm{T}}|^2 \,\mathrm{d}S,$$

where u_{s} is the scattering pattern corresponding to an exterior acoustic problem posed on Ω and Γ_{S} is the surface where scattering information is obtained. u_{T} is the measured scattering pattern. As in our previous work, the acoustic problem is interpreted as a constraint in the admissible values of the scattering pattern u_{s}, and the shape of the scatterer is represented by a B-spline curve. The positions of the control points of the curve are the parameters of the constrained optimization problem which is solved using a quasi-Newton-based optimization algorithm. This iterative algorithm requires at each step the computation of the derivative of the cost function with respect to the parameters of the optimization problem. In the following sections we show that this derivative is the discretized form of the shape derivative, i.e. the derivative of the cost function with respect to the domain Ω. The constraint posed by the scattering problem is removed by solving an adjoint system and an expression for the derivative is obtained in

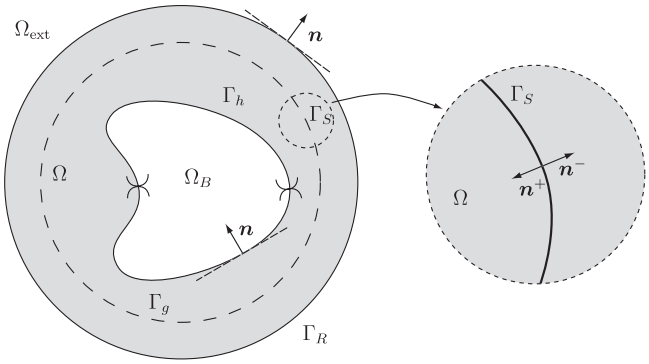

Figure 1. The domain of definition of the exterior acoustic problem.

terms of the solutions of these two problems. The adjoint problem is solved in an efficient manner by recognizing that it is composed of two fields, one which is obtained analytically, and another which is obtained numerically. The difficulties associated with far-field measurements are dealt with by investigating the behaviour of the analytical field. At each iteration, the main cost of the derivative calculation is independent of the number of parameters used to represent the scatterer since it is equal to the solution of two acoustic problems, a forward and an adjoint problem. The algorithm is implemented in a finite element framework and an efficient iterative method is used to solve the corresponding linear systems. Within each iteration of the optimization algorithm, a new search direction is calculated using a quasi-Newton update. The geometry of the scatterer is updated at each iteration using the new search direction.

An outline of the paper is as follows. In section 2 the strong and variational forms of the exterior acoustic problem are presented. Then in section 3 the concept of shape differentiation is introduced and used to calculate the shape derivative of a generic cost functional with the acoustic problem posed as a constraint. A closed form expression for the shape derivative is given next. To calculate the shape derivative an adjoint equation is solved using a decomposition technique that is described in section 4. Section 5 describes the discretization procedure used to calculate the components of the shape derivative vector. Finally, in section 6, the overall algorithm for the solution of the inverse problem is described. The algorithm uses a gradient-based optimization method to construct a sequence of control points that converge to the shape of the scatterer that minimizes the cost function. The gradient is computed using the approach described in the previous sections. Numerical results using synthetic noiseless data, data containing different levels of noise and data available at limited apertures are shown next. Finally, concluding remarks are given in section 7.

2. The exterior acoustic problem

Small perturbations of density and pressure in a homogeneous and quiescent ideal fluid are modelled by the wave equation. The time-harmonic solutions of the wave equation satisfy the Helmholtz equation. Further, in the case of an unbounded medium, it is required that all waves be outgoing at infinity. This constraint is called Sommerfeld's radiation condition [35] and mathematically ensures the uniqueness of the solution of the corresponding initial or boundary-value problem. The boundary-value problem corresponding to the exterior Helmholtz problem in d dimensions posed on the unbounded domain $\Omega_\infty = \Omega_{\text{ext}} \cup \Omega \subset \mathbb{R}^d$ (see figure 1) is given

as follows: find the total acoustic field $u = u_s + u_i$ such that

$$-\nabla^2 u - k^2 u = f \qquad \text{in } \Omega_\infty, \tag{1}$$

$$u = g \qquad \text{on } \Gamma_g, \tag{2}$$

$$\nabla u \cdot \boldsymbol{n} = h \qquad \text{on } \Gamma_h, \tag{3}$$

$$\lim_{r\to\infty} r^{(d-1)/2}\left(\frac{\partial u_s}{\partial r} - \mathrm{i}k u_s\right) = 0, \tag{4}$$

where u_s is the scattered field and u_i is the incident field which in our case will be given by

$$u_i(\boldsymbol{x}) = \exp(\mathrm{i}k\boldsymbol{x}\cdot\boldsymbol{d}), \tag{5}$$

$\boldsymbol{d}$ is the direction of the incident plane wave and k is the wavenumber. In (1)–(3) f is a prescribed external force, g is a prescribed Dirichlet boundary condition and h is a prescribed Neumann boundary condition. Equation (4) is the Sommerfeld boundary condition and $r = |\boldsymbol{x}|$.

Instead of working with the problem given by equations (1)–(4), we introduce a separable surface Γ_R which encloses the scatterer or radiator (here represented by the domain Ω_B with surface $\partial\Omega_B = \Gamma_g \cup \Gamma_h$) and any sources (i.e., outside Γ_R, f is identically zero) and impose the Dirichlet-to-Neumann (DtN) map [20] on Γ_R. In this work, this surface is either a circle for $d = 2$ or a sphere for $d = 3$. The corresponding boundary-value problem is given by: find $u = u_s + u_i$ such that

$$-\nabla^2 u - k^2 u = f \qquad \text{in } \Omega, \tag{6}$$

$$u = g \qquad \text{on } \Gamma_g, \tag{7}$$

$$\nabla u \cdot \boldsymbol{n} = h \qquad \text{on } \Gamma_h, \tag{8}$$

$$\nabla u_s \cdot \boldsymbol{n} = M(u_s) \qquad \text{on } \Gamma_R, \tag{9}$$

where (9) is the non-reflecting boundary condition imposed at Γ_R. The operator $M(u)$ can be represented as follows [20]:

$$M(u) = \sum_{n=N(d)}^{\infty} \sum_{j=-J(d)}^{J(d)} z_{|n|}(k, R)\psi_{nj}(\boldsymbol{x}) \int_{\Gamma_R} \psi_{nj}^*(\boldsymbol{x}_0) u(\boldsymbol{x}_0)\, \mathrm{d}\Gamma, \tag{10}$$

where an asterisk denotes the complex conjugate of a quantity and

$$N(d) = \begin{cases} -\infty & \text{if } d = 2, \\ 0 & \text{if } d = 3, \end{cases} \tag{11}$$

$$J(d) = \begin{cases} 0 & \text{if } d = 2, \\ n & \text{if } d = 3, \end{cases} \tag{12}$$

$$\psi_{nj}(\boldsymbol{x}) = \begin{cases} \sqrt{\dfrac{1}{2\pi R}}\exp(\mathrm{i}n\theta) & \text{if } d = 2, \\ \sqrt{\dfrac{(2n+1)(n-|j|)!}{4\pi R^2 (n+|j|)!}} P_n^{|j|}(\cos\theta)\exp(\mathrm{i}j\phi) & \text{if } d = 3, \end{cases} \tag{13}$$

$P_n^{|j|}$ is the associated Legendre function of degree n and order $|j|$, $\mathrm{d}\Gamma$ is the differential element corresponding to Γ_R. The impedance coefficients $z_{|n|}(k, R)$ are given by the following:

$$z_{|n|}(k, R) = \begin{cases} \dfrac{kH_{|n|}^{(1)'}(kR)}{H_{|n|}^{(1)}(kR)} & \text{if } d = 2, \\ \dfrac{kh_{|n|}^{(1)'}(kR)}{h_{|n|}^{(1)}(kR)} & \text{if } d = 3, \end{cases} \tag{14}$$

where $H_{|n|}^{(1)}$ is the Hankel function of the first kind of order $|n|$ and $h_{|n|}^{(1)}$ is the spherical Hankel function of the first kind of order $|n|$. $H_{|n|}^{(1)'}$ and $h_{|n|}^{(1)'}$ denote the derivatives of $H_{|n|}^{(1)}(\xi)$ and $h_{|n|}^{(1)}(\xi)$ with respect to the argument $\xi \in \mathbb{R}$, respectively. The boundary-value problem (6)–(9) is equivalent to (1)–(4).

The weak form associated with the boundary-value problem (6)–(9) is given by: find $u = u_\mathrm{i} + u_\mathrm{s} \in \mathcal{S}(\Omega)$ such that

$$a(\Omega; w, u) = \ell(\Omega; w) \qquad \forall w \in \mathcal{V}(\Omega), \tag{15}$$

where

$$a(\Omega; w, u) = (\nabla w, \nabla u)_\Omega - k^2(w, u)_\Omega - (w, M(u))_{\Gamma_\mathrm{R}}, \tag{16}$$

$$\ell(\Omega; w) = (w, f)_\Omega + (w, h)_{\Gamma_h} + (w, l)_{\Gamma_\mathrm{R}}, \tag{17}$$

$$(w, l)_{\Gamma_\mathrm{R}} = (w, \nabla u_\mathrm{i} \cdot \boldsymbol{n} - M(u_\mathrm{i}))_{\Gamma_\mathrm{R}}. \tag{18}$$

The inner products in (16) and (17) are defined by

$$(w, u)_\Omega = \int_\Omega w^* u \, \mathrm{d}\Omega, \tag{19}$$

$$(w, u)_{\Gamma_\mathrm{R}} = \int_{\Gamma_\mathrm{R}} w^* u \, \mathrm{d}\Gamma, \tag{20}$$

$$(w, u)_{\Gamma_h} = \int_{\Gamma_h} w^* u \, \mathrm{d}\Gamma, \tag{21}$$

where w^* denotes the complex conjugate of w. The set $\mathcal{S}(\Omega)$ and the linear space $\mathcal{V}(\Omega)$ are given by

$$\mathcal{S}(\Omega) = \{u \in H^1(\Omega); u(\boldsymbol{x}) = g(\boldsymbol{x}), \boldsymbol{x} \in \Gamma_g\}, \tag{22}$$

$$\mathcal{V}(\Omega) = \{u \in H^1(\Omega); u(\boldsymbol{x}) = 0, \boldsymbol{x} \in \Gamma_g\}. \tag{23}$$

From now on, we will call (15) the primal problem (also called the forward problem).

Remarks.

(1) In the case of a rigid scatterer, also called a sound-hard scatterer, $\Gamma_g = \emptyset$ and $h = 0$. This is the case we are mostly interested in.

(2) The variational form of the acoustic scattering problem presented here differs from the usual one. Note that problem (15) contains the total acoustic field u. Since the incident field u_i is known, it is common to formulate the problem such that we solve for the scattered field u_s only. Since the incident field u_i satisfies (6) with $f = 0$, the variational problem for u_s is given by: find u_s such that

$$(\nabla w, \nabla u_\mathrm{s})_\Omega - k^2(w, u_\mathrm{s})_\Omega - (w, M(u_\mathrm{s}))_{\Gamma_\mathrm{R}} = (w, f)_\Omega + (w, \tilde{h})_{\Gamma_h} \qquad \forall w \in \mathcal{V}(\Omega), \tag{24}$$

where $\tilde{h} = h - \nabla u_\mathrm{i} \cdot \boldsymbol{n}$. Note that, for the case of a rigid scatterer, $\tilde{h} \neq 0$. The reason behind using (15) instead of (24) is to obtain an expression for the shape derivative that is easier to implement numerically for the case of a rigid scatterer as we will see later.

3. Calculation of the shape derivative

To solve the inverse acoustic scattering problem we need to construct a functional that measures the difference between a trial solution and the measured scattered field corresponding to the target. In this work, we consider the case where this information is known on a ball of radius R_S, here denoted Γ_S, that encloses the object Ω_B and any sources. We then consider the following functional:

$$j(\Omega) = J(u(\Omega)) = \tfrac{1}{2}\int_{\Gamma_S} |u_s - u_T|^2 \, d\Gamma_S \tag{25}$$

where u_s satisfies the primal problem given by (15) and u_T is the measured scattered field on Γ_S. Even though we are limiting our presentation to this kind of functional, the procedure shown in this work can be readily applied to other types of functionals. In two dimensions, for example, we could know the scattered field at a number of points over the entire aperture. If the number of points is sufficiently large, and they are equispaced, we could interpolate the values to construct the function u_T and use (25) as the functional.

We are particularly interested in the limiting case as R_S goes to infinity, in which case the functional is given by

$$\hat{j}(\Omega) = \lim_{R_S\to\infty} j(\Omega) = \tfrac{1}{2}\int_{B_u} |\hat{u}_s - \hat{u}_T|^2 \, d\hat{\boldsymbol{x}}, \tag{26}$$

where B_u is the unit ball in $\mathbb{R}^d$ and $\hat{\boldsymbol{x}} = \boldsymbol{x}/|\boldsymbol{x}|$. $\hat{u}_s$ (or $\hat{u}_T$) denotes the far-field pattern corresponding to the scattered field u_s (or u_T) and satisfies the following relation:

$$u_s(\boldsymbol{x}) = \frac{\exp(ikr)}{r^{(d-1)/2}}\left(\hat{u}_s(\hat{\boldsymbol{x}}) + O\left(\frac{1}{r}\right)\right). \tag{27}$$

Note that functionals (25) and (26) depend implicitly on the shape of the domain Ω through u, the solution of the primal problem (15).

In this work we solve the inverse acoustic scattering problem by solving a shape optimization problem where the shape that minimizes the functional (25) or (26) subject to the constraint given by the primal problem (15) is the shape of the scatterer. Since we will use gradient-based optimization techniques to solve this constrained optimization problem, we need to develop an efficient procedure to calculate the shape derivative, i.e. the derivative with respect to the domain Ω.

To calculate the shape derivative, we use a methodology that is widely known in shape optimization [34]. First, we introduce a uniparametric family of mappings $\phi_\varepsilon = \phi_\varepsilon(\boldsymbol{V})$, such that every $\boldsymbol{x} \in \Omega$ is mapped to $\phi_\varepsilon(\boldsymbol{x}) = \boldsymbol{x}_\varepsilon$, where

$$\boldsymbol{x}_\varepsilon = \phi_\varepsilon(\boldsymbol{V})(\boldsymbol{x}) = \boldsymbol{x} + \varepsilon \boldsymbol{V}(\boldsymbol{x}), \tag{28}$$

$\varepsilon \in \mathbb{R}$, and $\boldsymbol{V}$ is a given smooth vector field in $\mathbb{R}^d$ that represents the direction of change of the domain. Note that by using the mapping (28), the domain Ω is mapped to the domain Ω_ε given by

$$\Omega_\varepsilon = \phi_\varepsilon(\Omega) = \{\boldsymbol{x}_\varepsilon | \boldsymbol{x}_\varepsilon = \boldsymbol{x} + \varepsilon \boldsymbol{V}(\boldsymbol{x}), \boldsymbol{x} \in \Omega\}. \tag{29}$$

We assume the mapping (28) tends to the identity mapping fast enough away from $\Gamma_g \cup \Gamma_h$. With this requirement we guarantee $\phi_\varepsilon(\Gamma_S) = \Gamma_S$ and $\phi_\varepsilon(\Gamma_R) = \Gamma_R$ since Γ_S and Γ_R are given fixed surfaces. We then define the shape derivative of any functional $j(\Omega)$ in the $\boldsymbol{V}$-direction, and denote it $Dj(\Omega)\cdot\boldsymbol{V}$, using the following expression:

$$Dj(\Omega)\cdot\boldsymbol{V} = \frac{d}{d\varepsilon} j(\Omega_\varepsilon)\bigg|_{\varepsilon=0}. \tag{30}$$

At this point, we could simply differentiate the expression (25) or (26) and obtain the shape derivative as follows:

$$Dj(\Omega)\cdot \boldsymbol{V} = D_u J(u(\Omega))\cdot \dot{u}, \tag{31}$$

where $D_u J$ is the derivative of the functional J with respect to its argument u, the dot in $D_u J(u(\Omega))\cdot \dot{u}$ represents the appropriate duality product and

$$\dot{u} = \frac{\mathrm{d}}{\mathrm{d}\varepsilon} u(\Omega_\varepsilon)\bigg|_{\varepsilon=0} \tag{32}$$

is obtained by differentiating the variational form (15) in the $\boldsymbol{V}$-direction and then solving the corresponding problems for $\dot{u}$. There will be one such problem for each direction of change of the domain Ω. Upon numerical discretization, the number of problems that need to be solved equals the number of parameters that are used to characterize the domain. An approach similar to this was used in [21].

In the following, we present an alternative method to compute the shape derivative (30) by solving an auxiliary equation, called the adjoint equation. It will be shown that using this *adjoint method* $\dot{u}$ does not need to be computed and as a consequence the cost of computing the shape derivative is independent of the number of parameters used to describe Ω, and therefore the shape of the scatterer.

We start by introducing the Lagrangian

$$\mathcal{L}(\Omega_\varepsilon;\lambda,u_\varepsilon) = J(u_\varepsilon) + \mathrm{Re}[a(\Omega_\varepsilon;\lambda,u_\varepsilon) - \ell(\Omega_\varepsilon;\lambda)] \tag{33}$$

where $\mathrm{Re}[b]$ denotes the real part of a complex quantity b and the subscript ε denotes that the corresponding field or domain has been deformed using mapping (28). $\lambda \in \mathcal{V}(\Omega_\varepsilon)$ is a Lagrange multiplier. The objective of this construction is to create a new function that assumes the same values as the original cost function if the constraint given by the primal problem is satisfied. Since the cost function is real-valued, we need to cast the extra terms (which can yield complex values) in (33) to real values. The operator $\mathrm{Re}[\cdot]$ is an obvious choice for this procedure. (The result obtained in the following derivation would not change if the imaginary part operator was used instead.) The field u_ε is the solution of the primal problem (15) posed in the 'deformed' configuration Ω_ε:

$$a(\Omega_\varepsilon;w,u_\varepsilon) = \ell(\Omega_\varepsilon;w) \qquad \forall w \in \mathcal{V}(\Omega_\varepsilon). \tag{34}$$

Under this mapping, the sesquilinear form $a(\Omega_\varepsilon;w,u_\varepsilon)$ and the linear form $\ell(\Omega_\varepsilon;w)$ correspond to

$$a(\Omega_\varepsilon;w,u_\varepsilon) = \int_{\Omega_\varepsilon} ((\partial_{\boldsymbol{x}_\varepsilon} w)^* \cdot (\partial_{\boldsymbol{x}_\varepsilon} u_\varepsilon) - k^2 w^* u_\varepsilon)\,\mathrm{d}\Omega_\varepsilon - \int_{\Gamma_\mathrm{R}} w^* M(u_\varepsilon)\,\mathrm{d}\Gamma, \tag{35}$$

$$\ell(\Omega_\varepsilon;w) = (w,f)_{\Omega_\varepsilon} + (w,h)_{\Gamma_{h\varepsilon}} + (w,l)_{\Gamma_\mathrm{R}}, \tag{36}$$

where $\Gamma_{h\varepsilon} = \phi_\varepsilon(\Gamma_h)$.

With the definitions above, we note that

$$J(u_\varepsilon) = \mathcal{L}(\Omega_\varepsilon;\lambda,u_\varepsilon) \qquad \forall \lambda \in \mathcal{V}(\Omega_\varepsilon). \tag{37}$$

As a consequence, the shape derivative can be computed as follows:

$$\begin{aligned} Dj(\Omega)\cdot\boldsymbol{V} &= \frac{\mathrm{d}}{\mathrm{d}\varepsilon} J(u_\varepsilon)\bigg|_{\varepsilon=0} && \text{(by definition (30)),}\\ &= \frac{\mathrm{d}}{\mathrm{d}\varepsilon} \mathcal{L}(\Omega_\varepsilon;\lambda,u_\varepsilon)\bigg|_{\varepsilon=0} && \text{(using (37)).} \end{aligned} \tag{38}$$

Note that u_0 corresponds to the solution of (34) at $\varepsilon = 0$ which is the primal problem (15). In the following, we choose the Lagrange multiplier λ such that $\dot{u}$ does not need to be computed in order to evaluate the shape derivative.

First note that, for a function $f : \mathbb{R} \to \mathbb{C}$, the following holds:

$$\frac{\mathrm{d}}{\mathrm{d}\varepsilon} \mathrm{Re}[f(\varepsilon)] = \mathrm{Re}\left[\frac{\mathrm{d}}{\mathrm{d}\varepsilon} f(\varepsilon)\right], \tag{39}$$

since $\varepsilon \in \mathbb{R}$. With this observation, and the linearity of the form $a(\Omega; w, u)$ on u, we get

$$\begin{aligned}\frac{\mathrm{d}}{\mathrm{d}\varepsilon}\mathcal{L}(\Omega_\varepsilon; \lambda, u_\varepsilon)\bigg|_{\varepsilon=0} &= \mathrm{Re}[D_1 a(\Omega; \lambda, u) \cdot \boldsymbol{V} - D_1 \ell(\Omega; \lambda) \cdot \boldsymbol{V}] \\ &+ \mathrm{Re}[a(\Omega; \lambda, \dot{u})] + D_u J(u) \cdot \dot{u},\end{aligned} \tag{40}$$

where D_1 denotes the derivative with respect to the first argument holding all other arguments fixed. For example

$$D_1 a(\Omega; \lambda, u) \cdot \boldsymbol{V} = \frac{\mathrm{d}}{\mathrm{d}\varepsilon} a(\Omega_\varepsilon; \lambda, u)\bigg|_{\varepsilon=0}. \tag{41}$$

The idea behind writing the shape derivative using (38) and (40) is to realize that the term $\dot{u}$ does not need to be computed if λ is selected such that it is the solution of the following variational problem:

$$\mathrm{Re}[a^*(\Omega; w, \lambda)] + D_u J(u) \cdot w = 0 \qquad \forall w, \tag{42}$$

where $a^*(\Omega; w, \lambda) = a(\Omega; \lambda, w)\ \forall w, \lambda$ is the adjoint of the sesquilinear form. Equation (42) is the so-called adjoint equation (the explicit form of the adjoint equation will be derived in the next subsection). Because of (42), the second line in (40) vanishes since $\dot{u}$ lives in the same space as w. Then, the expression for the shape derivative simplifies to

$$Dj(\Omega) \cdot \boldsymbol{V} = \mathrm{Re}[D_1 a(\Omega; \lambda, u) \cdot \boldsymbol{V} - D_1 \ell(\Omega; \lambda) \cdot \boldsymbol{V}]. \tag{43}$$

Note that the calculation of the shape derivative using expression (43) involves the solution of only two problems: the primal problem (15) and the adjoint problem (42). Once the primal field u and the Lagrange multiplier λ, which from now on we refer to as the *adjoint field*, are determined, we use expression (43) to calculate the shape derivative for any given direction $\boldsymbol{V}$ of change of the domain.

In the following, we explicitly calculate the terms in (42) and (43).

3.1. Explicit forms of the adjoint equation and shape derivative

We now calculate each of the terms that appear in the adjoint equation (42) and in the expression for the shape derivative given by (43). The basic idea is to transform all quantities that appear in these expressions back to the 'original configuration' Ω. Then the differentiation process is very similar to the differentiation of motions in continuum mechanics [18].

First, we define a tensor called the deformation gradient as follows:

$$F_\varepsilon = \nabla \phi_\varepsilon = I + \varepsilon \nabla \boldsymbol{V}. \tag{44}$$

With this definition, it is possible to show that gradients, volume elements and surface elements in the deformed configuration Ω_ε are related to the corresponding quantities defined in the original configuration Ω as follows

$$\partial_{x_\varepsilon} u = F_\varepsilon^{-\mathrm{T}} \nabla u, \tag{45}$$

$$\mathrm{d}\Omega_\varepsilon = \det F_\varepsilon \, \mathrm{d}\Omega, \tag{46}$$

$$\mathrm{d}\Gamma_\varepsilon = \det F_\varepsilon \| F_\varepsilon^{-\mathrm{T}} \boldsymbol{n} \| \, \mathrm{d}\Gamma. \tag{47}$$

Then it is straightforward to show the following results (for the derivation see [19]):

$$\frac{\mathrm{d}}{\mathrm{d}\varepsilon} F_\varepsilon \bigg|_{\varepsilon=0} = \nabla \boldsymbol{V}, \tag{48}$$

$$\frac{\mathrm{d}}{\mathrm{d}\varepsilon} (\partial_{\boldsymbol{x}_\varepsilon} u) \bigg|_{\varepsilon=0} = -\nabla \boldsymbol{V}^{\mathrm{T}} \nabla u, \tag{49}$$

$$\frac{\mathrm{d}}{\mathrm{d}\varepsilon} (\mathrm{d}\Omega_\varepsilon) \bigg|_{\varepsilon=0} = \operatorname{div} \boldsymbol{V}\, \mathrm{d}\Omega, \tag{50}$$

$$\frac{\mathrm{d}}{\mathrm{d}\varepsilon} (\mathrm{d}\Gamma_\varepsilon) \bigg|_{\varepsilon=0} = \operatorname{div}_\Gamma \boldsymbol{V}\, \mathrm{d}\Gamma, \tag{51}$$

where

$$\operatorname{div}_\Gamma \boldsymbol{V} = \operatorname{div} \boldsymbol{V} - \boldsymbol{n} \cdot (\nabla \boldsymbol{V}) \boldsymbol{n} \tag{52}$$

is the tangential divergence of the vector field $\boldsymbol{V}$.

Using these results we obtain

$$\begin{aligned} D_1 a(\Omega; \lambda, u) \cdot \boldsymbol{V} &= \frac{\mathrm{d}}{\mathrm{d}\varepsilon} \left[\int_{\Omega_\varepsilon} (\partial_{\boldsymbol{x}_\varepsilon} \lambda^* \cdot \partial_{\boldsymbol{x}_\varepsilon} u - k^2 \lambda^* u)\, \mathrm{d}\Omega_\varepsilon - \int_{\Gamma_{\mathrm{R}}} \lambda^* M(u)\, \mathrm{d}\Gamma \right]_{\varepsilon=0} \\ &= \int_\Omega (\nabla \lambda^* \cdot \nabla u - k^2 \lambda^* u) \operatorname{div} \boldsymbol{V}\, \mathrm{d}\Omega - \int_\Omega \nabla \lambda^* \cdot (\nabla \boldsymbol{V} + \nabla \boldsymbol{V}^{\mathrm{T}}) \nabla u\, \mathrm{d}\Omega. \end{aligned} \tag{53}$$

Likewise,

$$D_1 \ell(\Omega; \lambda) \cdot \boldsymbol{V} = \int_\Omega \lambda^* f \operatorname{div} \boldsymbol{V}\, \mathrm{d}\Omega + \int_\Omega \lambda^* \nabla f \cdot \boldsymbol{V}\, \mathrm{d}\Omega + \int_{\Gamma_h} \lambda^* h \operatorname{div}_\Gamma \boldsymbol{V}\, \mathrm{d}\Gamma + \int_{\Gamma_h} \lambda^* \dot{h}\, \mathrm{d}\Gamma, \tag{54}$$

where

$$\dot{h} = \frac{\mathrm{d}}{\mathrm{d}\varepsilon} h(\Omega_\varepsilon; \boldsymbol{x}_\varepsilon) \bigg|_{\varepsilon=0}. \tag{55}$$

In writing (55) we allow the Neumann boundary condition to explicitly depend on the shape of the domain. This is the case when h is of the form

$$h(\boldsymbol{x}) = \boldsymbol{v}(\boldsymbol{x}) \cdot \boldsymbol{n}(\boldsymbol{x}) \tag{56}$$

where $\boldsymbol{v}(\boldsymbol{x})$ is a known vector field and $\boldsymbol{n}$ is the normal to Γ_h at $\boldsymbol{x}$.

The term $D_u J(u) \cdot w$ is given by

$$D_u J(u) \cdot w = \mathrm{Re} \left[\int_{\Gamma_{\mathrm{S}}} (u_{\mathrm{s}} - u_{\mathrm{T}})^* w\, \mathrm{d}\Gamma \right]. \tag{57}$$

To calculate the term $a^*(\Omega; w, \lambda)$ in (42) we make use of $(f, g)_\Omega = (g, f)_\Omega^*$ to obtain

$$a^*(\Omega; w, \lambda) = (\nabla w, \nabla \lambda)_\Omega^* - k^2 (w, \lambda)_\Omega^* - (w, M^*(\lambda))_{\Gamma_{\mathrm{R}}}^*. \tag{58}$$

Therefore, the explicit form of the adjoint equation (42) is given by

$$(\nabla w, \nabla \lambda)_\Omega - k^2 (w, \lambda)_\Omega - (w, M^*(\lambda))_{\Gamma_{\mathrm{R}}} = -(w, u_{\mathrm{s}} - u_{\mathrm{T}})_{\Gamma_{\mathrm{S}}} \qquad \forall w \in \mathcal{V}(\Omega), \tag{59}$$

where the operator M^* is given by

$$M^*(\lambda) = \sum_{n=N(d)}^{\infty} \sum_{j=-J(d)}^{J(d)} z_{|n|}^*(k; R)\, \psi_{nj}(\boldsymbol{x}) \int_{\Gamma_{\mathrm{R}}} \psi_{nj}^*(\boldsymbol{x}_0) \lambda(\boldsymbol{x}_0)\, \mathrm{d}\Gamma. \tag{60}$$

Before we continue, we note that the DtN operator satisfies

$$(M^*(\lambda))^* = M(\lambda^*). \tag{61}$$

This result is easily obtained by conjugating all the terms in the right side of (60) and by noting that the summation in (60) is symmetric about $n = 0$ (for the case $d = 2$) or $j = 0$ (for the case $d = 3$).

It may appear that the variational form (59) is of a different type to the primal problem (15). Nevertheless, if we substitute w^* for w in (59), conjugate all terms and use the identity (61), we obtain the following *equivalent* form for the adjoint equation: find $\lambda^* \in \mathcal{V}(\Omega)$ such that

$$(\nabla w, \nabla\lambda^*)_\Omega - k^2(w, \lambda^*)_\Omega - (w, M(\lambda^*))_{\Gamma_R} = -(w, (u_s - u_T)^*)_{\Gamma_S} \qquad \forall w \in \mathcal{V}(\Omega). \tag{62}$$

Now, the adjoint equation (62) is of the same form as the primal problem (15).

Finally, we use (53) and (54) to obtain the expression of the shape derivative (43) in terms of domain integrals:

$$\begin{aligned} Dj(\Omega)\cdot\boldsymbol{V} = G(u,\lambda,\boldsymbol{V}) \\ = \operatorname{Re}\Bigg\{ &\int_\Omega (\nabla\lambda^*\cdot\nabla u - k^2\lambda^* u)\operatorname{div}\boldsymbol{V}\,\mathrm{d}\Omega - \int_\Omega \nabla\lambda^*\cdot(\nabla\boldsymbol{V} + \nabla\boldsymbol{V}^{\mathrm{T}})\nabla u\,\mathrm{d}\Omega \\ &- \int_\Omega \lambda^* f\operatorname{div}\boldsymbol{V}\,\mathrm{d}\Omega - \int_\Omega \lambda^*\nabla f\cdot\boldsymbol{V}\,\mathrm{d}\Omega - \int_{\Gamma_h} \lambda^* h\operatorname{div}_\Gamma\boldsymbol{V}\,\mathrm{d}\Gamma - \int_{\Gamma_h}\lambda^*\dot{h}\,\mathrm{d}\Gamma\Bigg\}. \end{aligned} \tag{63}$$

Remarks.

(1) In the method described above, we only need to solve two variational problems, (15) and (62), to calculate the functional derivative using (63). We also note that the primal and adjoint variational problems do not depend on the direction $\boldsymbol{V}$ of change of the domain. As a result, the cost of calculating the discrete approximation of the derivative does not depend on the number of parameters used to represent the domain, which is the main advantage of the adjoint approach over other methods.

(2) The primal and adjoint problems are of the same type. That structure can be exploited numerically: if the LU factors of the matrix corresponding to the discretized form of the variational equation are available, the solution of the adjoint problem amounts to an extra back-solve; if one uses an iterative solver, the matrix does not need to be reformed to solve the adjoint problem.

(3) Note that the numerical implementation of this method is not restricted to the DtN boundary condition. Other boundary conditions, such as the BGT [2], infinite elements [5] and the modified DtN map [17] can also be used. This is because in the development carried out so far, we have calculated an expression for the derivative that is independent of the discretization. We can use any type of numerical method to solve the primal and adjoint variational problems (15) and (62). In particular, we can use approximations to the Sommerfeld boundary condition instead of the DtN boundary condition in (15) and (62).

(4) As mentioned earlier, we will be particularly interested in the case of a scattering problem where $\Gamma_g = \emptyset$ and $h = 0$. In this case, the expression for the shape derivative simplifies to

$$\begin{aligned} Dj(\Omega)\cdot\boldsymbol{V} = \operatorname{Re}\Bigg\{ &\int_\Omega (\nabla\lambda^*\cdot\nabla u - k^2\lambda^* u)\operatorname{div}\boldsymbol{V}\,\mathrm{d}\Omega - \int_\Omega \nabla\lambda^*\cdot(\nabla\boldsymbol{V} + \nabla\boldsymbol{V}^{\mathrm{T}})\nabla u\,\mathrm{d}\Omega \\ &- \int_\Omega \lambda^* f\operatorname{div}\boldsymbol{V}\,\mathrm{d}\Omega - \int_\Omega \lambda^*\nabla f\cdot\boldsymbol{V}\,\mathrm{d}\Omega\Bigg\}. \end{aligned} \tag{64}$$

Note that in this case it is not necessary to calculate the surface gradients $\mathrm{div}_\Gamma \boldsymbol{V}$ and $\dot{h}$ to compute the shape derivative. This is why we pose the acoustic problem in the form (15) instead of the more usual form (24).

(5) It can be shown [34] that the derivative of any shape functional does not depend on the value of the vector field $\boldsymbol{V}$ inside Ω. It can also be shown that only the normal component $v_n = \boldsymbol{V} \cdot \boldsymbol{n}$ of the field $\boldsymbol{V}$ is relevant in the calculation. As a consequence, it is possible to write an expression for the shape derivative that contains only surface integrals. We will derive this expression for our particular case.
Starting with the expression (63), we integrate by parts the terms contained in the first, second and third lines so that we obtain expressions where $\boldsymbol{V}$ appears undifferentiated. For example, the first term in (63) is written as follows:

$$\int_\Omega \nabla\lambda^* \cdot \nabla u \,\mathrm{div}\, \boldsymbol{V}\, \mathrm{d}\Omega = \int_{\partial\Omega} (\nabla\lambda^* \cdot \nabla u)\,(\boldsymbol{V} \cdot \boldsymbol{n})\, \mathrm{d}\Gamma - \int_{\Omega\setminus\Gamma_S} \lambda^*_{,ij} u_{,i} V_j \,\mathrm{d}\Omega - \int_\Omega \lambda^*_{,i} u_{,ij} V_j \,\mathrm{d}\Omega. \tag{65}$$

Proceeding in the same manner for the remaining terms in (63), and using the fact that only the normal component of $\boldsymbol{V}$ on the boundary has a non-zero contribution in the shape derivative calculation, we arrive at the following expression:

$$\begin{aligned} Dj(\Omega)\cdot\boldsymbol{V} = \mathrm{Re}\Bigg\{ & \int_{\partial\Omega} (\nabla\lambda^* \cdot \nabla u - k^2\lambda^* u - \lambda^* f) v_n \,\mathrm{d}\Gamma \\ & - 2\int_{\partial\Omega} (\nabla\lambda^* \cdot \boldsymbol{n})(\nabla u \cdot \boldsymbol{n}) v_n \,\mathrm{d}\Gamma \\ & + \int_\Omega (\nabla\lambda \cdot \boldsymbol{V})\,(\nabla^2 u + k^2 u + f)\,\mathrm{d}\Omega \\ & + \int_{\Omega\setminus\Gamma_S} (\nabla u \cdot \boldsymbol{V})\,(\nabla^2\lambda + k^2\lambda)\,\mathrm{d}\Omega \\ & + \int_{\Gamma_h} \lambda^* h \,\mathrm{div}\, \boldsymbol{n} v_n \,\mathrm{d}\Gamma + \int_{\Gamma_h} \lambda^* \dot{h} \,\mathrm{d}\Gamma \Bigg\}. \end{aligned} \tag{66}$$

Finally, using the Euler–Lagrange equations corresponding to the primal problem (15) and the adjoint problem (62) we conclude that the integrands in the third and fourth line of (66) are identically zero. Using $\boldsymbol{V} = \boldsymbol{0}$ on Γ_R (since the DtN boundary is fixed) we rewrite the final expression for the shape derivative as follows:

$$\begin{aligned} Dj(\Omega)\cdot\boldsymbol{V} &= g(u, \lambda, v_n) \\ &= \mathrm{Re}\Bigg\{ \int_{\Gamma_h\cup\Gamma_g} (\nabla\lambda^* \cdot \nabla u - k^2\lambda^* u - \lambda^* f) v_n \,\mathrm{d}\Gamma \\ &\quad - 2\int_{\Gamma_h\cup\Gamma_g} (\nabla\lambda^* \cdot \boldsymbol{n})(\nabla u \cdot \boldsymbol{n}) v_n \,\mathrm{d}\Gamma + \int_{\Gamma_h} \lambda^* h \,\mathrm{div}\, \boldsymbol{n} v_n \,\mathrm{d}\Gamma + \int_{\Gamma_h} \lambda^* \dot{h} \,\mathrm{d}\Gamma \Bigg\}. \end{aligned} \tag{67}$$

As we pointed out, the shape derivative can be calculated using either an expression that involves domain integrals given by (63) or using (67). In the numerical examples shown in this work we have opted for the first approach, because for most discretization methods, gradients in the boundary are calculated with lower precision than inside the domain. As a consequence, (63) is better suited for the numerical approximation of the shape derivative.

4. Solving the adjoint problem

We now turn our attention to the solution of the adjoint variational problem (62). At first sight this problem can be solved using any numerical method. Nevertheless, it would be computationally inefficient to do so if the sampling boundary Γ_S is far away from the scatterer: since the DtN boundary has to contain any inhomogeneities, and that includes the right side term in (62), we would have to consider a domain that contains the boundary Γ_S and the discretization of this domain would introduce a large number of variables. Further, in the limiting case of functional (26), it is not clear how we would solve the corresponding variational problem.

We overcome these problems by constructing an additive decomposition of the adjoint field λ^*:

$$\lambda^* = \lambda_I + \lambda_S, \tag{68}$$

where λ_I is the analytical solution of a problem that contains the problematic source term and λ_S is the solution of an acoustic problem where the source term is not present. The advantages in solving the problem in this way instead of by the 'straightforward' solution of variational problem (62) are:

(1) since the problem for λ_S does not contain a source term, we can use a DtN surface closer to the scatterer, which in turn means that we have a smaller domain to discretize, and
(2) the limiting case is very easy to analyse since it will involve taking the limit $R_S \to \infty$ in the expression for λ_I.

We start the derivation of the equations for λ_I and λ_S by substituting (68) into (62) and writing the resulting terms as follows (see figure 1):

$$\begin{aligned}(\nabla w, \nabla\lambda_I)_{B_R} - k^2(w, \lambda_I)_{B_R} - (w, M(\lambda_I))_{\Gamma_R} - (\nabla w, \nabla\lambda_I)_{\Omega_B} + k^2(w, \lambda_I)_{\Omega_B} + (\nabla w, \nabla\lambda_S)_{\Omega} \\ - k^2(w, \lambda_S)_{\Omega} - (w, M(\lambda_S))_{\Gamma_R} = -(w, (u_s - u_T)^*)_{\Gamma_S} \qquad \forall w \in \mathcal{V}(\Omega),\end{aligned} \tag{69}$$

where $B_R = \Omega \cup \Omega_B$ is the ball of radius R. We now impose λ_I as the solution of the following variational equation:

$$(\nabla w, \nabla\lambda_I)_{B_R} - k^2(w, \lambda_I)_{B_R} - (w, M(\lambda_I))_{\Gamma_R} = -(w, (u_s - u_T)^*)_{\Gamma_S} \qquad \forall w. \tag{70}$$

It is important at this point to derive the Euler–Lagrange equations corresponding to (70). Integrating by parts the terms in (70) gives

$$\begin{aligned}- (w, \nabla^2\lambda_I)_{B_R\setminus\Gamma_S} + (w, \nabla\lambda_I^- \cdot \boldsymbol{n}^-)_{\Gamma_S} + (w, \nabla\lambda_I^+ \cdot \boldsymbol{n}^+)_{\Gamma_S} + (w, \nabla\lambda_I \cdot \boldsymbol{n})_{\Gamma_R} \\ - k^2(w, \lambda_I)_{B_R} - (w, M(\lambda_I))_{\Gamma_R} = -(w, (u_s - u_T)^*)_{\Gamma_S} \qquad \forall w,\end{aligned} \tag{71}$$

where $\boldsymbol{n}^+$ and $\boldsymbol{n}^-$ are defined in figure 1. $\nabla\lambda_I^{\pm}$ indicates that quantities are evaluated at $r = R_S \pm \delta$ with $\delta \to 0^+$, where r is the radial coordinate in a cylindrical or spherical system. Therefore, λ_I satisfies

$$-\nabla^2\lambda_I - k^2\lambda_I = 0 \qquad \text{in } B_R\setminus\Gamma_S, \tag{72}$$

$$[\![\nabla\lambda_I \cdot \boldsymbol{n}]\!] = -(u_s - u_T)^* \qquad \text{on } \Gamma_S, \tag{73}$$

$$\nabla\lambda_I \cdot \boldsymbol{n} = M(\lambda_I) \qquad \text{on } \Gamma_R, \tag{74}$$

where $[\![\nabla\lambda_I \cdot \boldsymbol{n}]\!] = \nabla\lambda_I^+ \cdot \boldsymbol{n}^+ + \nabla\lambda_I^- \cdot \boldsymbol{n}^-$. Problem (72)–(74) with the requirement that λ_I be continuous and bounded can be solved analytically. We consider separately the solutions for the cases $d = 2$ and 3 and study the limiting case when $R_S \to \infty$.

We start with the two-dimensional case. In the cylindrical coordinate system the solution of problem (72)–(74) is given by the following series:

$$\lambda_{\mathrm{I}}(r,\theta) = \begin{cases} \displaystyle\sum_{n=-\infty}^{\infty} \frac{1}{\sqrt{2\pi}} A_n J_{|n|}(kr)\exp(\mathrm{i}n\theta), & \text{for } 0 \leqslant r \leqslant R_{\mathrm{S}}, \\ \displaystyle\sum_{n=-\infty}^{\infty} \frac{1}{\sqrt{2\pi}} B_n H^{(1)}_{|n|}(kr)\exp(\mathrm{i}n\theta), & \text{for } R_{\mathrm{S}} \leqslant r < +\infty, \end{cases} \tag{75}$$

where

$$A_n = -\mathrm{i}\frac{\pi R_{\mathrm{S}}}{2} H^{(1)}_{|n|}(kR_{\mathrm{S}})a_n, \tag{76}$$

$$B_n = -\mathrm{i}\frac{\pi R_{\mathrm{S}}}{2} J_{|n|}(kR_{\mathrm{S}})a_n, \tag{77}$$

and a_n are the Fourier coefficients of $(u_{\mathrm{s}} - u_{\mathrm{T}})^*$, i.e.

$$a_n = \frac{1}{\sqrt{2\pi}} \int_0^{2\pi} \exp(-\mathrm{i}n\theta)(u_{\mathrm{s}} - u_{\mathrm{T}})^*(R_{\mathrm{S}},\theta)\,\mathrm{d}\theta. \tag{78}$$

We can now easily investigate the limiting case corresponding to functional (26). First, we investigate the behaviour of the function $(u_{\mathrm{s}} - u_{\mathrm{T}})^*$ for $R_{\mathrm{S}} \to +\infty$. Since u_{s} and u_{T} separately satisfy the exterior acoustic problem for some domain, this function is such that

$$(u_{\mathrm{s}} - u_{\mathrm{T}})^*(R_{\mathrm{S}},\theta) = \frac{\exp(-\mathrm{i}kR_{\mathrm{S}})}{\sqrt{R_{\mathrm{S}}}}\left((\hat{u}_{\mathrm{s}} - \hat{u}_{\mathrm{T}})^*(\theta) + \mathrm{O}\left(\frac{1}{R_{\mathrm{S}}}\right)\right), \tag{79}$$

where $(\hat{u}_{\mathrm{s}} - \hat{u}_{\mathrm{T}})^*(\theta)$ is the far-field pattern corresponding to $(u_{\mathrm{s}} - u_{\mathrm{T}})^*(r,\theta)$. Therefore,

$$a_n \sim \frac{\exp(-\mathrm{i}kR_{\mathrm{S}})}{\sqrt{R_{\mathrm{S}}}}\,\hat{a}_n \qquad \text{as } R_{\mathrm{S}} \to +\infty, \tag{80}$$

where $\hat{a}_n$ are the Fourier coefficients of $(\hat{u}_{\mathrm{s}} - \hat{u}_{\mathrm{T}})^*(\theta)$. We also know Hankel's asymptotic expansion for $H^{(1)}_{\nu}(\xi)$ for fixed ν ($\nu \in \mathbb{R}$) and $\xi \to +\infty$ (see [1, chapter 9]):

$$H^{(1)}_{\nu}(\xi) \sim \sqrt{\frac{2}{\pi\xi}}\,\exp(\mathrm{i}\chi), \tag{81}$$

where $\chi = \xi - \left(\frac{1}{2}\nu + \frac{1}{4}\right)\pi$. Therefore, from (76), (79) and (81) we have

$$\hat{A}_n = \lim_{R_{\mathrm{S}}\to+\infty} A_n = -\mathrm{i}\sqrt{\frac{\pi}{2k}}\exp\left[-\mathrm{i}\left(\frac{1}{2}|n| + \frac{1}{4}\right)\pi\right]\hat{a}_n, \tag{82}$$

and the final expression for λ_{I} for the case corresponding to functional (26) is given by

$$\lim_{R_{\mathrm{S}}\to+\infty} \lambda_{\mathrm{I}}(r,\theta) = \frac{1}{\sqrt{2\pi}} \sum_{n=-\infty}^{\infty} \hat{A}_n J_{|n|}(kr)\,\exp(\mathrm{i}n\theta), \qquad 0 \leqslant r < +\infty. \tag{83}$$

The three-dimensional case is treated similarly. In the spherical coordinate system, the solution of problem (72)–(74) with continuity and boundedness requirements for λ_{I} is

$$\lambda_{\mathrm{I}}(r,\theta,\phi) = \sum_{n=0}^{\infty} \sum_{j=-n}^{+n} b_{nj}(kr) Y_{nj}(\theta,\phi), \tag{84}$$

where $Y_{nj}(\theta,\phi)$ are the spherical harmonics

$$Y_{nj}(\theta,\phi) = \sqrt{\frac{(2n+1)(n-|j|)!}{4\pi(n+|j|)!}} P_n^{|j|}(\cos\theta)\exp(\mathrm{i}j\phi). \tag{85}$$

The radial functions $b_{nj}(kr)$ are similar to the two-dimensional case, but now they involve spherical Bessel functions

$$b_{nj}(kr) = \begin{cases} C_{nj}\, j_n(kr), & \text{for } 0 \leqslant r \leqslant R_S, \\ D_{nj} h_n^{(1)}(kr), & \text{for } R_S \leqslant r < +\infty, \end{cases} \tag{86}$$

where

$$C_{nj} = -\mathrm{i}k R_S^2 h_n^{(1)}(kR_S) a_{nj}, \tag{87}$$

$$D_{nj} = -\mathrm{i}k R_S^2 j_n(kR_S) a_{nj}, \tag{88}$$

and a_{nj} are the Fourier coefficients of $(u_s - u_T)^*$:

$$a_{nj} = \int_0^{2\pi} \int_0^{\pi} Y_{nj}^*(\theta, \phi)(u_s - u_T)^*(R_S, \theta, \phi) \sin\theta \, \mathrm{d}\theta \, \mathrm{d}\phi. \tag{89}$$

For the limiting case $R_S \to +\infty$ we have

$$a_{nj} \sim \frac{\exp(-\mathrm{i}kR_S)}{R_S} \hat{a}_{nj}, \qquad \text{as } R_S \to +\infty, \tag{90}$$

where $\hat{a}_{nj}$ are the Fourier coefficients of $(\hat{u}_s - \hat{u}_T)^*(\theta, \phi)$. Since the spherical Bessel's functions are related to the Bessel's functions of fractional order by

$$j_n(\xi) = \sqrt{\frac{\pi}{2\xi}} J_{n+1/2}(\xi), \tag{91}$$

$$h_n^{(1)}(\xi) = \sqrt{\frac{\pi}{2\xi}} H_{n+1/2}^{(1)}(\xi), \tag{92}$$

and using (81), (87) and (90)–(92), we can write the expression for λ_I for the case $R_S \to +\infty$ as follows:

$$\lim_{R_S \to +\infty} \lambda_I(r, \theta, \phi) = \sum_{n=0}^{+\infty} \sum_{j=-n}^{+n} \hat{C}_{nj} \frac{J_{n+1/2}(kr)}{\sqrt{r}} Y_{nj}(\theta, \phi), \tag{93}$$

where

$$\hat{C}_{nj} = -\mathrm{i}\sqrt{\frac{\pi}{2k}} \exp\left[-\mathrm{i}\left(\frac{1}{2}n + \frac{1}{2}\right)\pi\right] \hat{a}_{nj}. \tag{94}$$

We have derived an expression for λ_I for both the two- and three-dimensional cases and investigated the behaviour of the solution when $R_S \to +\infty$. This is a part of the adjoint field λ^*. We will now derive an equation for the remaining part, λ_S.

Given that λ_I satisfies (70), from (69) we conclude that λ_S has to satisfy the following variational problem:

$$(\nabla w, \nabla \lambda_S)_\Omega - k^2 (w, \lambda_S)_\Omega - (w, M(\lambda_S))_{\Gamma_R} = (\nabla w, \nabla \lambda_I)_{\Omega_B} - k^2 (w, \lambda_I)_{\Omega_B}$$
$$\forall w \in \mathcal{V}(\Omega). \tag{95}$$

We can simplify the expression above by integrating by parts the first term on the right side and using (72) to eliminate the volume integral. Then, the final variational equation for λ_S is given by: find $\lambda_S \in \tilde{\mathcal{S}}(\Omega)$ such that

$$(\nabla w, \nabla \lambda_S)_\Omega - k^2 (w, \lambda_S)_\Omega - (w, M(\lambda_S))_{\Gamma_R} = -(w, \nabla \lambda_I \cdot \boldsymbol{n})_{\Gamma_h} \qquad \forall w \in \mathcal{V}(\Omega), \tag{96}$$

where the set $\tilde{\mathcal{S}}(\Omega)$ is

$$\tilde{\mathcal{S}}(\Omega) = \{u \in H^1(\Omega);\ u = -\lambda_I \text{ on } \Gamma_g\}. \tag{97}$$

The set $\tilde{S}(\Omega)$ is defined as shown above because $\lambda \in \mathcal{V}(\Omega)$ which implies $\lambda^* = \lambda_I + \lambda_S = 0$ on Γ_g.

As mentioned in the beginning of this section, we are able to devise a scheme to calculate the adjoint field efficiently. That requires the *evaluation* of the field λ_I using (75) or (84) (or (83), (93) in the limiting case $R_S \to +\infty$) and the solution of an acoustic problem, given by (96), with non-homogeneous Neumann data and without a distributed source term.

We now have all the ingredients necessary to calculate the shape derivative. Algorithm 4.1 summarizes the steps for calculating the shape derivative of functional (25) while algorithm 4.2 summarizes the steps for calculating the shape derivative of (26).

Algorithm 4.1. Shape derivative calculation for functional (25).

(1) Solve the acoustic problem (15) to evaluate u.
(2) Calculate the incident part λ_I of the adjoint field using (75) if $d = 2$ or (84) if $d = 3$.
(3) Solve problem (96) to calculate the scattered part λ_S of the adjoint field.
(4) Calculate the adjoint field: $\lambda^* = \lambda_I + \lambda_S$.
(5) Calculate the shape derivative using (63) or (67).

Algorithm 4.2. Shape derivative calculation for functional (26).

(1) Solve the acoustic problem (15) to evaluate u.
(2) Calculate the incident part λ_I of the adjoint field using (83) if $d = 2$ or (93) if $d = 3$.
(3) Solve problem (96) to calculate the scattered part λ_S of the adjoint field.
(4) Calculate the adjoint field: $\lambda^* = \lambda_I + \lambda_S$.
(5) Calculate the shape derivative using (63) or (67).

Remarks.

(1) The procedure described in this section is not limited to functionals (25) or (26). In particular, any functional where the sampling surface Γ_S is a spheroid (prolate or oblate) may be treated in exactly the same form. The incident part λ_I of the adjoint field λ^* is obtained analytically using spheroidal angular and radial wavefunctions (see [1, chapter 21]). The adjoint field is then computed by summing λ_I with the solution of problem (96) where the natural boundary condition, given by the term $-(w, \nabla\lambda_I \cdot \boldsymbol{n})_{\Gamma_h}$, is changed accordingly. Obviously, the limiting case corresponding to the far-field pattern will reduce to the expressions previously derived.
We can also easily modify the results in this section to include the case where the sampling surface Γ_S is not closed. For example, we could consider having only limited aperture information, say, from angle θ_i to angle θ_f, in functional (26) so that the new functional is given by

$$\hat{J}(\Omega) = \tfrac{1}{2}\int_{\theta_i}^{\theta_f} |\hat{u}_s - \hat{u}_T|^2 \,\mathrm{d}\theta. \tag{98}$$

We can now rewrite this expression in the following form:

$$\hat{J}(\Omega) = \tfrac{1}{2}\int_{0}^{2\pi} |\hat{u}_s - \hat{u}_T|^2 \delta_\chi \,\mathrm{d}\theta, \tag{99}$$

where $\delta_\chi : [0, 2\pi] \to \{0, 1\}$ is the indicator function for the set $\chi = [\theta_i, \theta_f]$, i.e., it assumes the value 1 in χ and the value 0 in $[0, 2\pi]\backslash\chi$. The shape derivative calculation follows the same steps as for the functional (26). In particular, the incident part λ_I of the adjoint field is given by expressions (82) and (83) where the Fourier coefficients $\hat{a}_n$ are now given by

$$\hat{a}_n = \frac{1}{\sqrt{2\pi}}\int_{0}^{2\pi} \exp(-\mathrm{i}n\theta)(\hat{u}_s - \hat{u}_T)^*(\theta)\delta_\chi(\theta) \,\mathrm{d}\theta. \tag{100}$$

(2) We can use the methodology developed above to treat problems where information is available only at a finite number of sampling points and from multiple incident waves. For example, in three dimensions, we can consider the functional

$$j(\Omega) = \tfrac{1}{2} \sum_{j=1}^{n_{\mathrm{sp}}} \sum_{i=1}^{n_{\mathrm{iw}}} |u_{\mathrm{s}}^{i}(\boldsymbol{x}_j) - u_{\mathrm{T}\,j}^{i}|^2, \tag{101}$$

where n_{sp} is the number of sampling points, i.e., the number of points in the domain where acoustic information is available, and n_{iw} is the number of incident plane waves at different directions of illumination. The superscript i indicates solutions or measurements corresponding to the ith incident direction and the subscript j indicates that these are obtained at the jth sampling point. For a single incident plane wave, the incident part of the adjoint field is simple to calculate and is given by

$$\lambda_{\mathrm{I}}(\boldsymbol{x}) = -\sum_{j=1}^{n_{\mathrm{sp}}} (u_{\mathrm{s}}(\boldsymbol{x}_j) - u_{\mathrm{T}\,j})^{*} \Phi(\boldsymbol{x}, \boldsymbol{x}_j) \tag{102}$$

where, in three dimensions, Φ is the radiating fundamental solution of the Helmholtz equation given by

$$\Phi(\boldsymbol{x}, \boldsymbol{x}_j) = \frac{1}{4\pi} \frac{\mathrm{e}^{\mathrm{i}k|\boldsymbol{x}-\boldsymbol{x}_j|}}{|\boldsymbol{x}-\boldsymbol{x}_j|}, \qquad \boldsymbol{x} \neq \boldsymbol{x}_j. \tag{103}$$

With this result, we calculate the scattered part of the adjoint field using (96) and λ^{*} is then calculated by summing these two contributions. For $n_{\mathrm{iw}} > 1$ we need to calculate one adjoint field for each incident plane wave. If we define u^i to be the primal solution corresponding to the ith incident wave and λ^i the corresponding adjoint solution, calculated as shown above, the shape derivative of functional (101) becomes

$$Dj(\Omega) \cdot \boldsymbol{V} = \sum_{i=1}^{n_{\mathrm{iw}}} G(u^i, \lambda^i, \boldsymbol{V}) = \sum_{i=1}^{n_{\mathrm{iw}}} g(u^i, \lambda^i, v_n), \tag{104}$$

where the expressions for $G(u^i, \lambda^i, \boldsymbol{V})$ and $g(u^i, \lambda^i, v_n)$ are given by (63) and (67), respectively. Note that, even though we need to calculate one adjoint field λ^i and one primal field u_{i} for each incident direction, these fields are the solutions of variational problem (96) with different right side terms. We can exploit this observation in the numerical solution. For example, a block version of an iterative Krylov subspace algorithm can be used to solve the corresponding linear system with multiple right-hand sides.

5. Numerical approximation of the shape derivative

Algorithms 4.1 and 4.2 enumerate the steps in the calculation of the shape derivative using the adjoint formulation developed in the previous sections. In this section, we discuss its numerical approximation and implementation in a finite element framework. For this development, we need to address each of the ingredients necessary to calculate the shape derivative: the numerical approximation of the primal and adjoint fields; the discretization of the boundary corresponding to the scatterer $\partial\Omega_{\mathrm{B}}$ and the definition of the corresponding vector field $\boldsymbol{V}$; and the calculation of the shape derivative using either (63) or (67).

The finite element method is used to solve the variational problem (15) for the numerical approximation u^h of the primal field u. Likewise, the same discretization is used to solve (96) for λ_{S}^h which is the numerical approximation of λ_{S}. The linear systems corresponding to the finite element discretization of the primal and adjoint variational problems are solved using an efficient method developed by Oberai *et al* [28, 29].

The incident part of the conjugate of the adjoint field, given by λ_{I}^h, is calculated using a truncated form of expressions (75) or (83) in the two-dimensional case, or (84) or (93) in the three-dimensional case. This field is calculated at each nodal point of the finite element mesh used in the solution of the primal and adjoint problems and interpolated using the same interpolation functions. Then, the numerical approximation of the adjoint field, given by λ^h, is obtained by conjugating the sum of the contributions λ_{I}^h and λ_{S}^h.

The boundary $\partial\Omega_{\mathrm{B}}$ of the domain where the primal and adjoint problems are posed is constructed by patching together a set of geometrical primitives in a CAD modeller. For example, in the two-dimensional case we can use lines, arcs, B-splines or NURBS curves to represent the boundary. Correspondingly, in the three-dimensional case, we can use planes, ellipsoidal patches and B-spline, Bézier or NURBS surfaces. In the two-dimensional examples shown in this work, $\partial\Omega_{\mathrm{B}}$ is discretized using quadratic closed B-splines, i.e. the boundary is parametrized using the following form (see [27, chapter 5]):

$$\boldsymbol{x}(s) = \sum_{i=0}^{n} N_{i,3}(s)\boldsymbol{x}_i \tag{105}$$

where $\boldsymbol{x}(s)$ is the position of a point in $\partial\Omega_{\mathrm{B}}$, $n+1$ is the number of control points of the quadratic B-spline, $N_{i,3}$ is the shape function (using the notation introduced in [27]) corresponding to the ith control point $\boldsymbol{x}_i$, and s is a real number such that $0 \leqslant s \leqslant n-1$. From the expression above, we conclude that the boundary $\partial\Omega_{\mathrm{B}}$ is uniquely characterized by $2 \times (n+1)$ parameters given by each component of the $n+1$ control points of the curve.

With this definition for the shape of the boundary, and from (28), we define the numerical approximation $\boldsymbol{V}^h$ of the vector field $\boldsymbol{V}$ on $\partial\Omega_{\mathrm{B}}$ as

$$\begin{aligned}\boldsymbol{V}^h(\boldsymbol{x}(s)) &= \sum_{i=0}^{n}\sum_{k=1}^{2}(N_{i,3}(s)\boldsymbol{e}_k)V_{ik} \\ &= \sum_{i=0}^{n}\sum_{k=1}^{2}\boldsymbol{\varphi}_{ik}(s)V_{ik}\end{aligned} \tag{106}$$

where $\boldsymbol{e}_k$ is the kth unit vector in the Cartesian coordinate system. This defines a linear space for the set of admissible vector fields $\boldsymbol{V}^h$, where the basis is given by $\{\boldsymbol{\varphi}_{ik}(s)|i = 0, \ldots, n;\ k = 1, 2\}$, with $\boldsymbol{\varphi}_{ik}(s) = N_{i,3}(s)\boldsymbol{e}_k$. While such an expression is appropriate for the computation of the shape derivative using (67), it is not appropriate for a computation that involves domain integrals such as (63) since $\boldsymbol{V}(\boldsymbol{x})$ in not defined in the interior of Ω. As we mentioned earlier, it can be shown that the value of the derivative in (63) is insensitive to the extension of $\boldsymbol{V}$ to the interior of the domain Ω. We use this result to arbitrarily choose an extension for the elements $\boldsymbol{\varphi}_{ik}$ and therefore define the value of $\boldsymbol{V}$ in Ω. In this work we choose this extension as the solution of an auxiliary elasticity-type boundary-value problem posed on a subset of Ω, which we denote Ω_{BL} (see figure 2). The problem is given by: find $\boldsymbol{v}_{ik}(\boldsymbol{x})$, $i = 0, \ldots, n$, $k = 1, 2$, such that

$$\operatorname{div} T = \boldsymbol{0} \qquad \text{in } \Omega_{\mathrm{BL}}, \tag{107}$$

$$\boldsymbol{v}_{ik} = N_{i,3}\boldsymbol{e}_k \qquad \text{on } \partial\Omega_{\mathrm{B}}, \tag{108}$$

$$\boldsymbol{v}_{ik} = \boldsymbol{0} \qquad \text{on } \partial\Omega_{\mathrm{BL}}\backslash\partial\Omega_{\mathrm{B}}, \tag{109}$$

where

$$T = 2\mu\epsilon + \lambda\epsilon_{ii}\boldsymbol{I}, \tag{110}$$

$$\epsilon = \tfrac{1}{2}(\nabla\boldsymbol{v}_{ik} + \nabla\boldsymbol{v}_{ik}^{\mathrm{T}}), \tag{111}$$

and the parameters μ and λ are given by

$$\mu = \frac{E}{2(1+\nu)}, \tag{112}$$

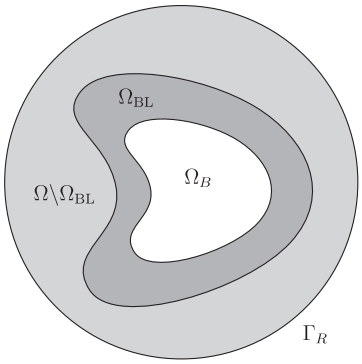

Figure 2. Ω_{BL} is chosen as a small part of the domain Ω. It is constructed by choosing a small number of layers of finite elements surrounding $\partial\Omega_{\mathrm{B}}$.

$$\lambda = \frac{\nu E}{(1+\nu)(1-2\nu)}. \tag{113}$$

The solution to problem (107)–(109) is a smooth vector field that decays to zero away from $\partial\Omega_{\mathrm{B}}$. We use $E = 1.0$ and $\nu = 0.3$ in all the numerical examples shown in the next section. Then, each element of the basis is given by

$$\boldsymbol{\varphi}_{ik}(\boldsymbol{x}) = \begin{cases} \boldsymbol{v}_{ik}(\boldsymbol{x}) & \text{if } \boldsymbol{x} \in \Omega_{\mathrm{BL}}, \\ \mathbf{0} & \text{if } \boldsymbol{x} \in \Omega\backslash\Omega_{\mathrm{BL}}. \end{cases} \tag{114}$$

The finite element method is used to solve the $2 \times (n+1)$ boundary-value problems (107)–(109). The same mesh that is used in the solution of the primal and adjoint problems is used in the solution of the extension problem, but the subdomain Ω_{BL} is such that it contains only a small number of layers of finite elements in the vicinity of $\partial\Omega_{\mathrm{B}}$. In our calculations we found that ten layers of elements were enough to obtain accurate results. We should also mention that the extension problem does not need to be solved accurately, since in the continuous limit any extension yields the same value for the shape derivative. Therefore, in our calculations, (107)–(109) were not solved to full precision (we required a relative tolerance of only 10^{-3} in the iterative solution of the extension problem). For all these reasons, the numerical solution of all the extension problems is insignificant when compared to the time required to solve a single primal or adjoint problem.

Finally, the discrete form or approximate form of the shape derivative is constructed by inserting u^h, λ^h and $\boldsymbol{V}^h$ into (63) or (67). The linearity of these forms with respect to the vector field $\boldsymbol{V}$ yields

$$\begin{aligned} Dj(\Omega)^h \cdot \boldsymbol{V}^h &= \sum_{i=0}^{n}\sum_{k=1}^{2} G_{ik} V_{ik} \\ &= \sum_{i=0}^{n}\sum_{k=1}^{2} G(u^h, \lambda^h, \boldsymbol{\varphi}_{ik}) V_{ik}, \end{aligned} \tag{115}$$

$$\begin{aligned} Dj(\Omega)^h \cdot \boldsymbol{V}^h &= \sum_{i=0}^{n}\sum_{k=1}^{2} g_{ik} V_{ik} \\ &= \sum_{i=0}^{n}\sum_{k=1}^{2} g(u^h, \lambda^h, \boldsymbol{\varphi}_{ik} \cdot \boldsymbol{n}) V_{ik}. \end{aligned} \tag{116}$$

The quantities $G_{ik} = G(u^h, \lambda^h, \varphi_{ik})$ or $g_{ik} = g(u^h, \lambda^h, \varphi_{ik} \cdot \boldsymbol{n})$ are the components of the shape derivative vector. As will be seen in the next section, this vector is supplied to an optimization algorithm which is used in the solution of the inverse problem.

It can be shown that the straightforward implementation of (115) provides a better approximation for the shape derivative than (116) if the gradients in the boundary are calculated by simply differentiating the finite element solutions. For this reason, we use expression (115) to calculate the components of the shape derivative in the numerical examples shown in the next section.

6. Inverse acoustic scattering problem

6.1. Problem description and solution algorithms

We consider the problem of identifying the shape of a rigid object from the knowledge of its far-field scattering pattern obtained in response to plane waves incident at a specified angle and at certain frequencies. This problem is somewhat different to what is commonly considered in the literature [4, 9, 24], where plane waves with different incident directions and of a single frequency are used to illuminate the body. As discussed in remark 2 of section 4 this case can also be treated with our technique and will be considered at a later date.

The body is assumed to be a rigid scatterer, so $\Gamma_g = \emptyset$. The direction of the incident plane wave is $\boldsymbol{d} = -(1/\sqrt{2})(1, 1)$. No other sources are present in the problem; thus $f = 0$. The far-field patterns corresponding to incident plane waves with wavenumbers $k = 0.5$, 1.0, 1.5, 2.0 and 2.5 are known over the entire aperture (in some of the numerical examples only a part of this information is utilized). These far-field patterns are generated numerically by solving an exterior acoustic problem for a given scatterer, called the *target*. Polar plots of absolute values of the far-field patterns corresponding to each of these wavenumbers are shown in figure 3. The first 81 Fourier modes of the scattering pattern are used in the computation of λ_I; i.e. the series (83) is truncated at $n = \pm 40$.

Given this far-field information and the direction of the incident wave, the algorithm attempts to find the shape of the scattering object.

The solution of this inverse problem is accomplished in five 'stages'. At each stage, an optimization algorithm is used to find the shape of the scatterer that minimizes the functional

$$j(\Omega; k) = \tfrac{1}{2} \int_0^{2\pi} |\hat{u}_s(\theta; k) - \hat{u}_T(\theta; k)|^2 \, d\theta \tag{117}$$

where $\hat{u}_s(\cdot; k)$ is the far-field pattern corresponding to the scattered part of the solution of the acoustic problem (15) and $\hat{u}_T(\cdot; k)$ is the given (or measured) scattering pattern. The initial guess in each stage is given by the shape of the scatterer obtained in the previous stage. Every subsequent stage uses information at a higher wavenumber. The idea behind this heuristic is to allow the algorithm to progressively recover finer details of the geometry of the scatterer.

For the first stage in the algorithm, the initial guess is given by a closed quadratic B-spline curve obtained by equally spacing 16 control points on a square of unit dimensions centred at the origin of the coordinate system. The target is a closed quadratic B-spline curve with 17 control points. Figure 4 shows the position of the control points for the curves representing the initial guess and the target object.

The solution of the optimization problem posed at each stage is accomplished by the NPSOL optimization program [15] which implements a method based on sequential quadratic programming (SQP) [14, 16, 31]. The basic structure of an SQP method involves two types of iteration: major and minor iterations. In the major iterations a sequence designed to converge to a point that satisfies the first-order optimality conditions is constructed. The construction of this

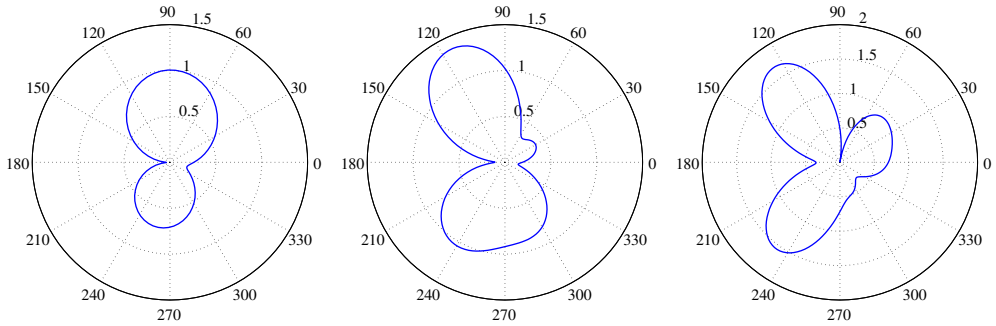

(a) $k = 0.5$ (b) $k = 1.0$ (c) $k = 1.5$

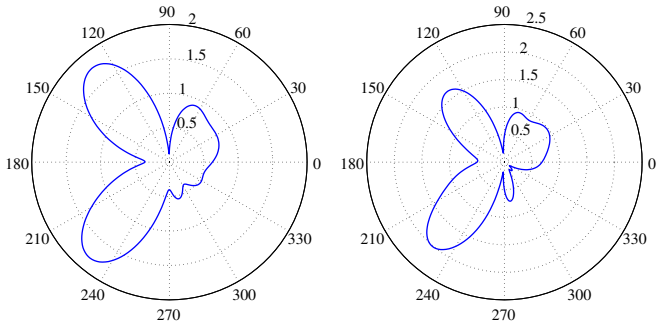

(d) $k = 2.0$ (e) $k = 2.5$

Figure 3. Far-field scattering patterns corresponding to illumination of the target object with plane waves of different wavenumbers k and incident direction $\boldsymbol{d} = -(1/\sqrt{2})(1, 1)$.

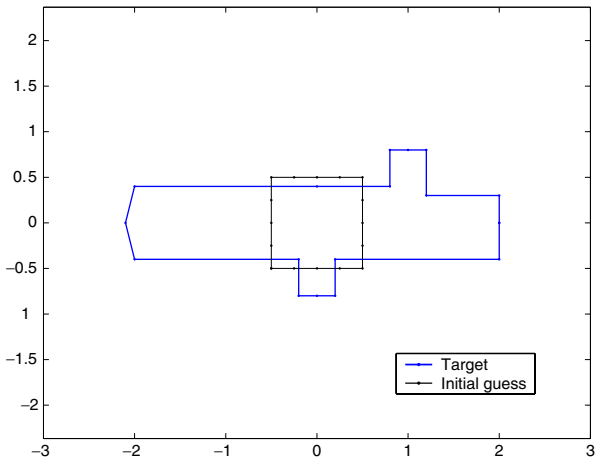

Figure 4. Control points of the curves representing the initial guess and the target object.

sequence involves finding a search direction that is the solution of a quadratic subproblem (QP) (which is a quadratic approximation of the nonlinear problem). The solution of the QP is achieved in an iterative fashion: these are the minor iterations in the algorithm. Once the search direction is found, the major iteration looks for a step length that produces a sufficient

decrease in a so-called merit function that measures how much closer the point is to the optimum.

In our case, within both major and minor iterations of the NPSOL program, the cost function (117) and its derivatives with respect to each of the control points have to be supplied. These derivatives are the components G_{ik} of the shape derivative vector which is computed using (115).

Every step in the optimization algorithm requires movement of the control points of the curve corresponding to the scatterer's surface and therefore the construction of a new finite element mesh. A mesh generation program using a Delaunay triangulation scheme [36] was constructed to automize this procedure. At each stage in the algorithm the mesh size was selected such that the number kh, which is related to the average number of elements per wavelength, was kept constant at $kh = 0.2$ ($\approx$30 elements per wavelength). In order to accommodate large deformations of the surface corresponding to the scattering object, a scheme was devised such that two consecutive supporting segments of the B-spline were not allowed to have very disparate sizes. In this scheme, whenever a segment was found to be larger than three times the size of one of its neighbours, a new control point was inserted at the mid-point of that segment. This technique ensured a homogeneous distribution of control points along the curve. It also caused the number of control points used to represent the scatterer's surface to grow during the solution of the inverse problem. For instance, in the first example presented below, the surface initially had 16 control points, while the surface corresponding to the converged solution is composed of 24 control points. The increase in the number of control points has no effect in the cost of the computation since the cost of calculating the shape derivative using the adjoint method is independent of this number.

An important parameter in the NPSOL program is the relative function precision ϵ_{R} (see [15]), which is the relative precision of the functional value calculation. This parameter tells the optimization program that it should not attempt to distinguish between functional values that differ by less than the error inherent in the calculation. ϵ_{R} clearly depends on the accuracy of the finite element computation and in the following numerical examples we used $\epsilon_{\mathrm{R}} = 10^{-4}$. This means that the first four significant digits in the functional calculation are correct. By adjusting this parameter it is possible to 'mimic' a discrepancy principle and to use the same algorithm to solve problems with noisy measurements, as shown in section 6.5.

6.2. Full aperture problem

In this example, the scattering information shown in figure 3 is available over the entire aperture; i.e. $\hat{u}_{\mathrm{T}}(\theta)$ is known for $\theta \in [0, 2\pi]$.

Figure 5 shows the behaviour of the functional values at each stage of the algorithm. A total of 112 iterations were required to solve this inverse problem. The numbers of steps required to solve the minimization problem posed at each stage were 15, 10, 22, 36 and 29. It is important to note that most of the computational effort is spent in the final stages of the algorithm where, due to larger values of the wavenumber, the mesh is finer. For example, while the mesh corresponding to the initial step contained only 751 nodes, the mesh corresponding to the last step had 10 585 nodes. This means that, for the purpose of computing the total cost of the algorithm, one can disregard the cost associated with the initial stages (lower wavenumbers). Nevertheless, the information contained at lower wavenumbers is crucial for the reconstruction algorithm as it provides a good initial point for the algorithm at higher wavenumbers.

Figure 6 shows the initial guess for the shape of the scattering object and the converged shapes at each stage of the algorithm. Figures 6(a)–(f) show the absolute value of the adjoint field on the computational domain. The colour map is kept constant across all the figures with

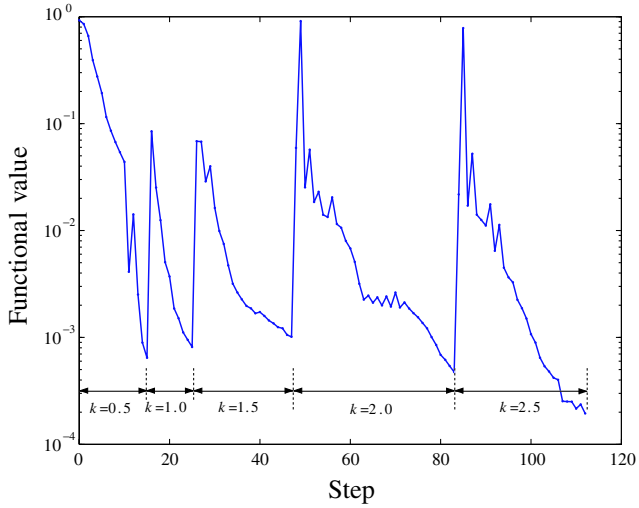

Figure 5. Evolution of the functional value at each step in the solution of the inverse problem.

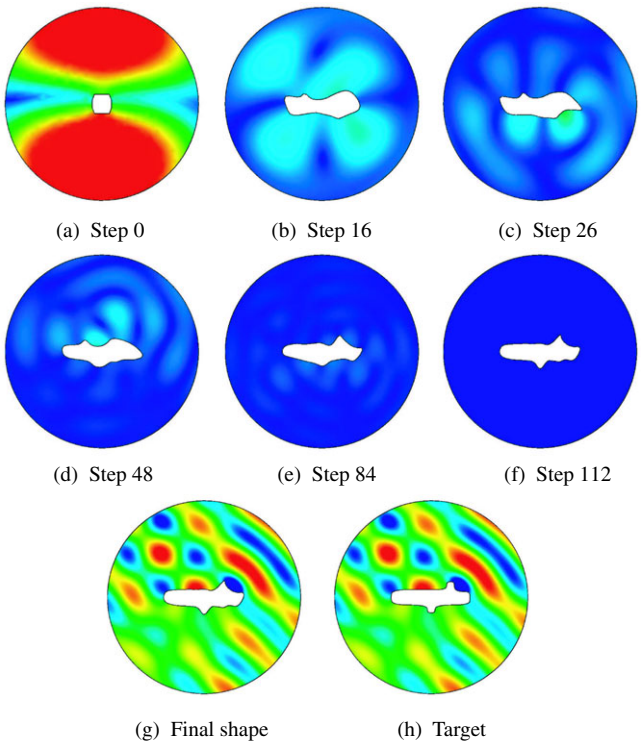

Figure 6. The series of steps taken by the algorithm in the full aperture case.
M An AVI movie of this figure is available from stacks.iop.org/IP/20/199.

warmer colours (red) representing higher values and colder colours (blue) representing lower values[5]. A figure where colder colours predominate indicates lower values of the adjoint

[5] Note to the reader. Please refer to the online version of this article for the correct colour scheme in the figures. In the printed version of the article the colours are mapped to grey tones.

field and that the corresponding solution is closer to the optimal one. Figures 6(g) and (h) show the total acoustic field corresponding to the final solution and the target calculated at the highest wavenumber. The similarity of the acoustic fields in these figures is another measure of convergence of the algorithm.

It should be noted that the algorithm was able to recover the correct size and width of the scattering object. In addition, the two features present in the object were successfully recovered. Their relative placement and generic dimensions agree very well with the target. It is also remarkable that the feature in the shadow zone was accurately recovered. Figures 6(a)–(d) show that at lower wavenumbers the main dimensions of the object were reconstructed very well with figure 6(d) already indicating some recovery of the remaining features. Steps 84 and 112, which correspond to the converged solutions at wavenumbers $k = 2.0$ and 2.5, show that information from higher wavenumbers is used to recover further details from the target object. It should also be noted that even at the highest wavenumber, the wavelength of the incident field is several times that of a representative length associated with the features in the target. At $k = 2.5$ this ratio is approximately 6. One would expect that the reconstruction scheme would not be able to accurately capture geometric details that are much smaller than the wavelength. Nevertheless, as seen in figures 6(g) and (h), the algorithm was still able to reconstruct the object and its features accurately.

A word about the cost of the overall calculation using this adjoint-based method: the total number of problems solved up to convergence is 224 (one primal and one adjoint problem for each step). As was previously said, the cost of the algorithm is independent of the number of control points used to represent the surface of the scatterer. By comparison, if a central finite difference scheme was used to calculate the derivatives, a total of 7581 acoustic calculations would be needed to solve this inverse problem (the break-up of this calculation involves multiplying the total number of control points used to represent the scatterer at each step by three and summing these quantities).

The total time required to solve this inverse problem using the adjoint-based method developed in this work is about 25 min using a single 1.9 GHz Pentium 4 processor.

6.3. Partial aperture problem

The inverse problem of the previous section is considered with scattering information available only over partial apertures. All other data in the problem are kept the same. For this case, the functional to be minimized at each stage of the algorithm is

$$j(\Omega; k) = \tfrac{1}{2} \int_0^{\Delta} |\hat{u}_s(\theta; k) - \hat{u}_T(\theta; k)|^2 \, \mathrm{d}\theta. \tag{118}$$

The target object is the same as in the previous example; therefore the far-field patterns shown in figure 3 are valid. Two cases are considered here: $\Delta = \pi$ and $\pi/2$.

6.3.1. Case $\Delta = \pi$. This case corresponds to having the scattering information shown in figure 3 available in the range $0 \leqslant \theta \leqslant \pi$. Figure 7 shows the corresponding solution. As in the previous example, the same colour map was used when plotting the absolute value of the adjoint field in figures 7(a)–(f). This shows how the surface of the scatterer evolves towards the final solution. Figures 7(g) and (h) show the final shape obtained by the algorithm and the target object as well as the corresponding acoustic fields. Note that the size and width of the scattering surface are in good agreement with those of the target object. It should also be noted that the general dimensions, and position relative to the object, of the protrusion in its upper part are recovered with quality comparable to the full aperture case. The protrusion

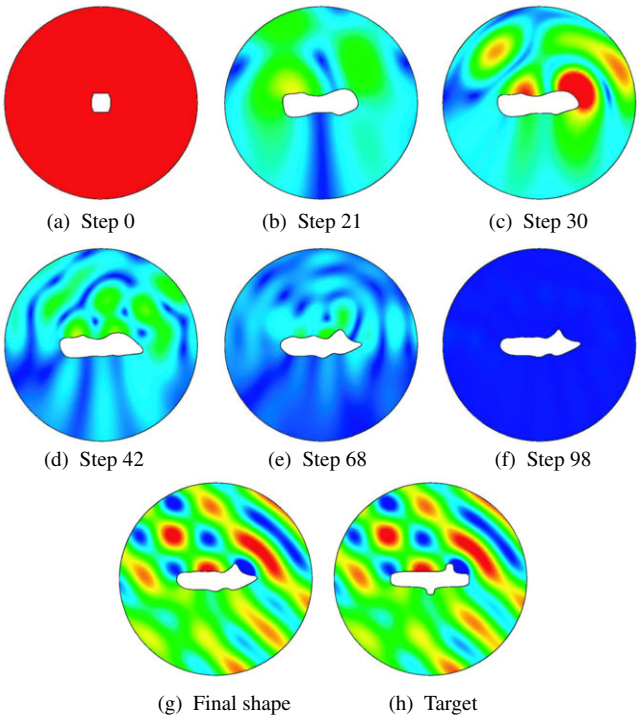

Figure 7. The sequence of steps in the calculation involving scattering information over a limited aperture ($\Delta = \pi$).

on the lower part of the object is not recovered which is not a surprise given that scattering information from the lower hemisphere is not available.

6.3.2. Case $\Delta = \pi/2$. Only scattering information from the first quadrant is available in this example. The solution for this case is presented in figure 8. The same colour map was used when plotting the absolute value of the adjoint field in figures 8(a)–(f). From figures 8(g) and (h), it can be seen that the algorithm was again able to recover the size and width of the target object quite well and only a small part of the protrusion on the upper part of the scatterer.

6.4. Effect of the direction of the incident plane wave

In the previous examples, the incident direction of the plane waves was kept constant. For the same target, and using the entire aperture, the effect of the incident direction on the solution of the inverse problem is investigated in this example.

Figure 9 shows the final shape obtained by the algorithm and the total acoustic field around the scatterer for different choices of the angle of illumination θ_i. Given the direction $\boldsymbol{d} = (d_1, d_2)$ of the incident plane waves, the angle of illumination θ_i is defined by $\theta_i = \arctan(d_2/d_1)$. $\theta_i = 5\pi/4$ corresponds to the case considered in section 6.2. With the exception of the reconstructions corresponding to $\theta_i = \pi/2$ and $3\pi/2$ the results of the other reconstructions are somewhat similar in that the general dimensions of the target object and the two protrusions are recovered. The cases $\theta_i = 3\pi/4$ and $7\pi/4$ show features with sharp corners close to the protrusion on the lower part of the body. The corners appear

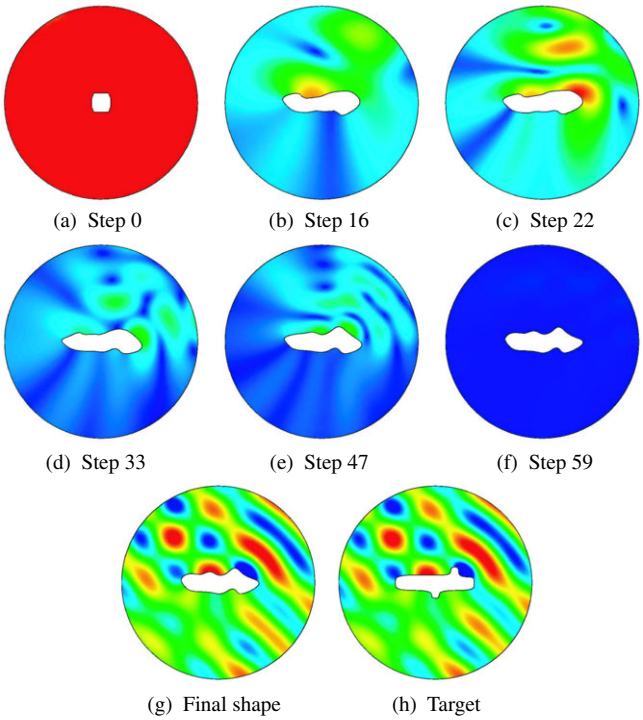

Figure 8. The sequence of steps in the calculation involving scattering information over a limited aperture ($\Delta = \pi/2$).

because, during the iterative process, some of the control points became very close to each other and the optimization algorithm is not able to separate them. This may be avoided by constraining the maximum change in curvature at each point during the optimization process.

The cases corresponding to $\theta_i = \pi/2$ and $3\pi/2$ show a degradation in the quality of the reconstructions when compared to other directions. While the final shapes have approximately the same size and width as the target, the protrusions are barely present in the reconstructed shape. The reason for this behaviour is partially related to the fact that only far-field information is used to solve the inverse problem, so the additional signal produced by a protrusion aligned with the direction of illumination is very weak.

6.5. Behaviour of the algorithm with noisy data

In this example, the method is tested for stability with respect to random noise added to the data. Like in [24], a random number in the interval $[-\gamma, \gamma]$ is added to the real and imaginary parts of the Fourier coefficients of the far-field scattering pattern $\hat{u}_T$. The noise level ϵ is defined as

$$\epsilon^2 = \frac{\int_0^{2\pi} \gamma^2 \, d\theta}{\int_0^{2\pi} |\hat{u}_T|^2 \, d\theta}. \tag{119}$$

In [24], Kress and Rundell used a convergence criteria in the optimization algorithm that mimicked a discrepancy principle by terminating the iterations when a normalized value of the cost function achieves 0.6ϵ. While this scheme can also be used here, a different strategy was selected to solve this problem.

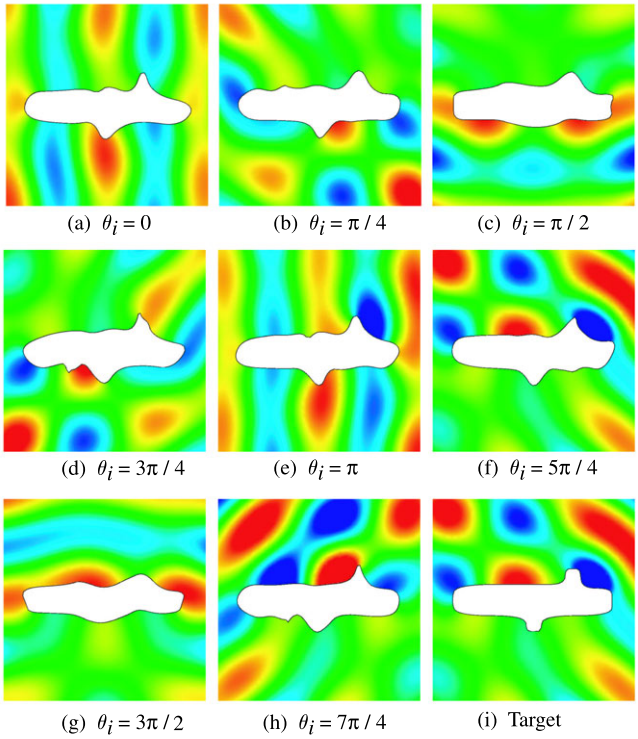

Figure 9. Scattering objects obtained for different angles (θ_i) of the incident plane waves.

Our strategy is based on selecting the appropriate value of the function precision, ϵ_R, in the optimization solver, based on the level of noise in the data. As explained before (see section 6), ϵ_R reflects the relative precision of the cost function calculation. In the case of noiseless data, the value $\epsilon_R = 10^{-4}$ was used. This means that, for the level of accuracy used to solve these problems (which, among other parameters, depends on the number kh) the cost function is calculated with four digits of accuracy. The optimization algorithm does not distinguish two scatterers with cost functions that differ by less than the error inherent in the calculation. This provides a practical scheme for stopping the iterative process.

In the case of noise present in the data, the value of ϵ_R also depends on the level of noise. Assuming that multiple realizations of the measurements satisfy a Gaussian distribution, this value is calculated by measuring the L^2-norm of the scattering pattern for each measurement and by computing the mean, $\hat{x}$, and standard deviation, σ, for several realizations. The value $3\sigma/\hat{x}$ is then chosen as the relative function precision due only to noise. (The '3' is used so that the algorithm does not distinguish the mean from approximately 99% of the realizations.) Then this value is summed to the error inherent in the discretization to define ϵ_R.

The example shown in section 6.2 is revisited (the plane waves have an incident angle $\theta_i = 5\pi/4$ and scattering information is available over the entire aperture) and three noise levels are considered: $\epsilon = 1\%, 3\%$ and 5%. The values for ϵ_R used in the reconstructions are shown in table 1. The final results are shown in figure 10 where the solution corresponding to noiseless data and the target shape are also displayed. It is easy to discern the degradation of the quality of the reconstruction with increased level of noise; nevertheless, even at 5% noise, the algorithm recovers with good precision the length and width of the object and the features

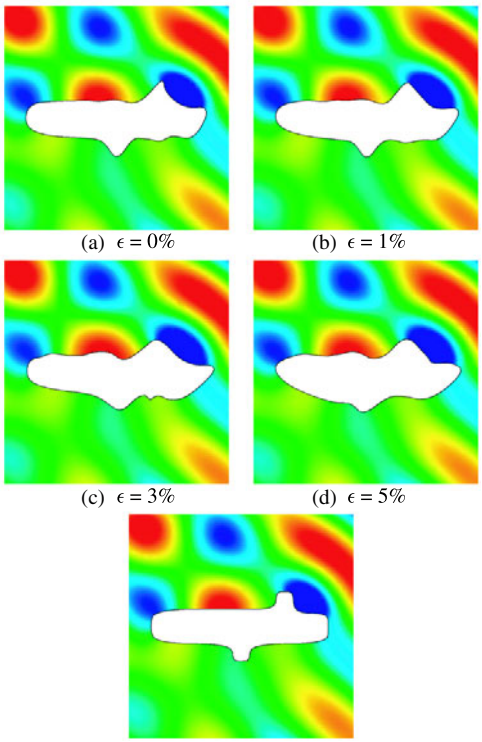

(a) $\epsilon = 0\%$ (b) $\epsilon = 1\%$

(c) $\epsilon = 3\%$ (d) $\epsilon = 5\%$

(e) Target

Figure 10. Final solutions corresponding to different noise levels (ϵ) in the measurements.

Table 1. Values used for ϵ_R based on the level of noise, ϵ, in the data.

ϵ (%)	0	1	3	5
ϵ_R	1×10^{-4}	3×10^{-3}	1×10^{-2}	2×10^{-2}

present in the upper and lower part. The number of iterations necessary to solve these problems changes with the level of noise. While 112 iterations are required to solve the problem for the case $\epsilon = 0\%$, the algorithm takes 75 iterations in the case $\epsilon = 1\%$, 60 iterations for $\epsilon = 3\%$ and 60 iterations for $\epsilon = 5\%$.

7. Conclusions

We have developed and implemented an efficient algorithm to solve inverse acoustic scattering problems. In this work the inverse problem is posed in the general framework of a constrained optimization problem with a cost functional that measures the difference between a trial solution and measured scattering information and a constraint given by the exterior acoustic boundary-value problem (or equivalently, its variational equation). The domain that minimizes the functional under this constraint is the solution of the inverse problem.

To solve the optimization problem efficiently, functional derivatives are required. These derivatives are calculated using the adjoint approach developed in this work. The cost of the computation is independent of the number of parameters used to represent the shape of the scatterer (in this case the parameters are control points of a B-spline curve that describes the

shape of the scattering object) and the cost is equivalent to the computation of an extra exterior acoustic problem, the adjoint problem.

The reconstructions presented in this work show the effectiveness of this method in treating several types of inverse acoustic scattering problems. The algorithm was tested in several situations: first, far-field scattering information was made available over the entire aperture, then limited aperture problems were considered; in a third example the object was illuminated by plane waves of different incident directions, and finally the algorithm was tested using noisy data. In all cases the proposed method was able to recover the shape of the scattering object.

Acknowledgments

Sandia is a multiprogramme laboratory operated by Sandia Corporation, a Lockheed Martin Company, for the United States Department of Energy under contract DE-AC04-94AL85000. This work was partially supported by ONR under contract N00014-99-1-0121 with Stanford University.

References

[1] Abramowitz M and Stegun I A (ed) 1976 *Handbook of Mathematical Functions* 9th edn (New York: Dover)
[2] Bayliss A, Gunzburger M and Turkel E 1982 Boundary conditions for the numerical solution of elliptic equations in exterior domains *SIAM J. Appl. Math.* **42** 439–51
[3] Brandfass M and Langenberg K J 1992 Review of progress in quantitative nondestructive evaluation *Polarimetric Microwave Inverse Scattering as Applied to Nondestructive Testing* ed D E Chimenti and D O Thompson (New York: Plenum)
[4] Brandfass M, Langerman A D and Warnick K F 2001 A comparison of the Colton–Kirsch inverse scattering methods with tomographic inverse scattering *Inverse Problems* **17** 1797–816
[5] Burnett D S 1994 A three-dimensional acoustic infinite element based on a prolate spheroidal multipole expansion *J. Acoust. Soc. Am.* **96** 2798–816
[6] Cakoni F and Colton D 2003 Combined far-field operators in electromagnetic inverse scattering theory *Math. Methods Appl. Sci.* **26** 413–29
[7] Colton D, Coyle J and Monk P 2000 Recent developments in inverse acoustic scattering theory *SIAM Rev.* **42** 369–414
[8] Colton D, Giebermann K and Monk P 2000 A regularized sampling method for solving three-dimensional inverse scattering problems *SIAM J. Sci. Comput.* **21** 2316–30
[9] Colton D and Kirsch A 1996 A simple method for solving inverse scattering problems in the resonance region *Inverse Problems* **12** 383–93
[10] Colton D and Piana M 1998 The simple method for solving the electromagnetic inverse scattering problem: the case of te polarized waves *Inverse Problems* **14** 597–614
[11] Colton D, Piana M and Potthast R 1997 A simple method using Morozov's discrepancy principle for solving inverse scattering problems *Inverse Problems* **13** 1477–93
[12] Dorn O, Miller E L and Rappaport C M 2000 A shape reconstruction method for electromagnetic tomography using adjoint fields and level sets *Inverse Problems* **16** 1119–56
[13] Feijóo G R, Malhotra M, Oberai A A and Pinsky P M 2001 Shape sensitivity calculations for exterior acoustics problems *Eng. Comput.* **18** 376–91
[14] Fletcher R 2000 *Practical Methods of Optimization* 2nd edn (New York: Wiley)
[15] Gill P E, Murray W, Saunders M A and Wright M H 2001 User's guide for NPSOL 5.0: a FORTRAN package for nonlinear programming *Stanford Optimization Laboratory Technical Report* 86-6 Stanford (Revised 4 June 2001)
[16] Gill P E, Murray W and Wright M H 1981 *Practical Optimization* (New York: Academic)
[17] Grote M J and Keller J B 1995 On non-reflecting boundary conditions *J. Comput. Phys.* **122** 231–43
[18] Gurtin M E 1981 *An Introduction to Continuum Mechanics* (*Mathematics in Science and Engineering* vol 158) (New York: Academic)
[19] Haug E J, Choi K K and Komkov V 1986 *Design Sensitivity Analysis of Structural Systems* (*Mathematics in Science and Engineering* vol 177) (New York: Academic)
[20] Keller J B and Givoli D 1989 Exact non-reflecting boundary conditions *J. Comput. Phys.* **82** 172–92

[21] Kirsch A 1993 The domain derivative and two applications in inverse scattering theory *Inverse Problems* **9** 81–96
[22] Kirsch A 1998 Characterization of the shape of a scattering obstacle using the spectral data of the far field operator *Inverse Problems* **14** 1489–512
[23] Kirsch A 1999 Factorization of the far-field operator for the inhomogeneous medium case and an application to inverse scattering theory *Inverse Problems* **15** 413–29
[24] Kress R and Rundell W 1994 A quasi-Newton method in inverse obstacle scattering *Inverse Problems* **10** 1145–57
[25] Kress R and Zinn A 1992 On the numerical solution of the three dimensional inverse obstacle scattering problem *J. Comput. Appl. Math.* **42** 49–61
[26] Litman A, Lesselier D and Santosa F 1998 Reconstruction of a two-dimensional binary obstacle by controlled evolution of a level-set *Inverse Problems* **14** 685–706
[27] Mortenson M E 1997 *Geometric Modeling* 2nd edn (New York: Wiley)
[28] Oberai A A 1998 On modeling the large-scale exterior acoustics problem using the finite-element method *PhD Thesis* Stanford University, CA, USA
[29] Oberai A A, Malhotra M and Pinsky P M 1998 On the implementation of the Dirichlet-to-Neumann radiation condition for iterative solution of the Helmholtz equation *Appl. Numer. Math.* **27** 443–64
[30] Potthast R 1994 Fréchet differentiability of boundary integral operators in inverse acoustic scattering *Inverse Problems* **10** 431–47
[31] Powell M J D 1983 Mathematical programming: the state of the art *Variable Metric Methods for Constrained Optimization* ed A Bachem, M Grötschel and B Korte (Berlin: Springer) pp 288–311
[32] Ramananjaona C, Lambert M, Lesselier D and Zolesio J P 2001 Shape reconstruction of buried obstacles by controlled evolution of a level set: from a min–max formulation to numerical experimentation *Inverse Problems* **17** 1087–111
[33] Santosa F 1996 A level-set approach for inverse problems involving obstacles *ESAIM: Control Optim. Calculus Variat.* **1** 17–33
[34] Sokolowski J and Zolesio J-P 1992 *Introduction to Shape Optimization: Shape Sensitivity Analysis* (*Springer Series in Computational Mathematics* vol 16) (Berlin: Springer)
[35] Sommerfeld A 1912 The Green's function of the oscillation equation *Jahresber. Deutsch. Math. Ver.* **21** 309–53
[36] Thompson J F, Soni B K and Weatherill N P (ed) 1999 *Handbook of Grid Generation* (Boca Raton, FL: CRC Press)